4-7-2023

Primary bilateral macronodular adrenocortical hyperplasia (PBMAH) patient with ARMC5 mutations.

Peng Tang

Jun Zhang

Song Peng

Xuzhi Yan

Yapeng Wang

See next page for additional authors

CANCER

PHF8-GLUL axis in lipid deposition and tumor growth of clear cell renal cell carcinoma

Song Peng[1]†, Ze Wang[1]†, Peng Tang[1]†, Shuo Wang[1]†, Yiqiang Huang[1], Qiubo Xie[2], Yapeng Wang[1], Xintao Tan[1], Tang Tang[1], Xuzhi Yan[1], Jing Xu[1], Weihua Lan[1], Luofu Wang[1], Dianzheng Zhang[3], Bin Wang[4], Tiejun Pan[2], Jun Qin[1,5]*, Jun Jiang[1]*, Qiuli Liu[1]*

For clear cell renal cell carcinoma (ccRCC), lipid deposition plays important roles in the development, metastasis, and drug resistance. However, the molecular mechanisms underlying lipid deposition in ccRCC remain largely unknown. By conducting an unbiased CRISPR-Cas9 screening, we identified the epigenetic regulator plant homeodomain finger protein 8 (PHF8) as an important regulator in ccRCC lipid deposition. Moreover, PHF8 is regulated by von Hippel–Lindau (VHL)/hypoxia-inducible factor (HIF) axis and essential for VHL deficiency–induced lipid deposition. PHF8 transcriptionally up-regulates glutamate-ammonia ligase (GLUL), which promotes the lipid deposition and ccRCC progression. Mechanistically, by forming a complex with c-MYC, PHF8 up-regulates TEA domain transcription factor 1 (TEAD1) in a histone demethylation–dependent manner. Subsequently, TEAD1 up-regulates GLUL transcriptionally. Pharmacological inhibition of GLUL by L-methionine sulfoximine not only repressed ccRCC lipid deposition and tumor growth but also enhanced the anticancer effects of everolimus. Thus, the PHF8-GLUL axis represents a potential therapeutic target for ccRCC treatment.

INTRODUCTION

About 430,000 people suffer from and more than 179,000 die of kidney cancer each year worldwide, and these numbers have been increasing in the past decades (*1*). Clear cell renal cell carcinoma (ccRCC) characterized by increased lipid deposition in the cytoplasm accounts for more than 75% of all subtypes of kidney cancer (*2*). It has been well established that the intracellular lipid droplets mainly composed of triglycerides and cholesterol esters play important roles in energy homeostasis, membrane synthesis, and cellular signaling during proliferation (*3*). More recent evidence indicates that extra lipid deposition in ccRCC is involved not only in tumor initiation and progression but also in metastasis and resistance to the antiangiogenic drug (*4*, *5*).

Inactivation of von Hippel–Lindau (VHL) caused by either somatic mutation or promoter methylation occurs in ~90% of ccRCC (*6*). Loss of function of VHL leads to accumulation of hypoxia-inducible factors (HIFs), the major driving force in ccRCC development (*7*). In addition, metabolic reprogramming driven by VHL/HIF-mediated pseudo-hypoxia makes ccRCC a metabolism-related disease (*8*, *9*) evidenced by increased glucose usage (Warburg effect) and extra lipid deposition (*3*). Multiple lines of evidence showed that aberrant activation of VHL/HIF axis is the main cause of lipid deposition (*3*, *10*). However, the underlying mechanism in VHL/HIF-mediated lipid deposition in ccRCC remains to be revealed.

Glutamine is the most abundant amino acid in the blood stream and involves in multiple metabolic pathways (*11*). Comparing to noncancer cells, increased accumulation and metabolism of glutamine in cancer cells (*2*) can serve as a precursor for tricarboxylic acid (TCA) cycle and the syntheses of lipids, glutathione, and nonessential amino acids (*12*), providing a metabolic fuel to sustain rapid cancer cell proliferation, progression, and metastasis (*11*, *13*). In VHL-deficient cells including ccRCC, glutamine is the major source for lipid synthesis via reductive carboxylation (*8*, *14*). Although exogenously supplied glutamine favors lipid deposition and tumor cell growth, the endogenously produced glutamine plays indispensable roles in multiple metabolic pathways (*15*, *16*). Glutamate-ammonia ligase (GLUL), also known as glutamine synthase, is the only identified enzyme responsible for de novo glutamine synthesis by ligating a glutamate with an ammonium ion (NH_4^+) (*12*). Previous studies have showed that GLUL-mediated glutamine synthesis plays a crucial role in tumor growth via regulating amino acid transportation and nitrogen metabolism such as nucleotide synthesis and recycling excessive ammonia (*17*, *18*), whereas the roles of GLUL in ccRCC are unclear.

It has been reported that dysfunction of epigenetic regulators including *PBRM1*, *SETD2*, *BAP1*, and *KDM5C* are associated with ccRCC (*19*). Alterations of the VHL/HIF axis is known to affect several Jumonji C (JmjC)-containing epigenetic regulators (*20*, *21*), including plant homeodomain finger protein 8 (PHF8), also known as KDM7B. PHF8 transcriptionally regulates target gene expression by demethylating H3K9me2/1, H3K27me2, or H4K20me1 (*22*, *23*) and involves in neuronal differentiation, cognitive ability development, cell adhesion, and cytoskeleton organization (*24*–*26*). More recent data suggest that up-regulated PHF8 is correlated with a variety of malignancies including breast cancer (*27*), gastric cancer (*28*), hepatocellular carcinoma (*29*), acute lymphoblastic leukemia (*30*), and prostate cancer (*31*). In this study, we demonstrated

[1]Department of Urology, Daping Hospital, Army Medical University, Chongqing 400042, P.R. China. [2]Department of Urology, Chinese PLA General Hospital of Central Theater Command, Wuhan, Hubei, P.R. China. [3]Department of Biomedical Sciences, Philadelphia College of Osteopathic Medicine, 4170 City Avenue, Philadelphia, PA 19131, USA. [4]Department of Gastroenterology & Chongqing Key Laboratory of Digestive Malignancies, Daping Hospital, Army Medical University, Chongqing 400042, P.R. China. [5]CAS Key Laboratory of Tissue Microenvironment and Tumor, CAS Center for Excellence in Molecular Cell Science, Shanghai Institute of Nutrition and Health Sciences, Chinese Academy of Sciences, University of Chinese Academy of Sciences, Shanghai, P.R. China.
*Corresponding author. Email: liuqiuli900827@163.com (Q.L.); jiangjun_64@163.com (J.J); qinjun@sibs.ac.cn (J.Q.)
†These authors contributed equally to this work.

that PHF8 promotes lipid deposition and tumor growth in ccRCC. Mechanistically, PHF8 is recruited by c-MYC to the promoter regions of TEA domain transcription factor 1 (*TEAD1*) to transcriptionally up-regulate TEAD1. Subsequently, TEAD1 up-regulates GLUL transcriptionally. In addition, we have demonstrated that targeting the PHF8-GLUL axis not only inhibited lipid deposition and tumor growth of ccRCC but also synergized with the therapeutic reagent everolimus (EVE).

RESULTS

A CRIPSR-Cas9 screen reveals a key role of PHF8 in the lipid deposition of ccRCC

Given the important roles of lipid deposition and epigenetic reprogramming in ccRCC, we decided to investigate whether epigenetic regulators are involved in ccRCC lipid deposition. To this end, we first carried out an unbiased CRISPR-Cas9 screening of 1136 epigenetic regulators with four small guide RNAs (sgRNAs) per gene (table S1). The 786-O cells (VHL-null cells) were transfected with the sgRNA pool, followed by BODIPY 493/503 staining and flow cytometry to sort the cells into two subpopulations based on the levels of cellular fatty acid (Fig. 1A). The primary screening identified 39 genes (table S2) exhibiting altered sgRNA frequencies ($P < 0.05$; Fig. 1B). Furthermore, results from real-time quantitative polymerase chain reaction (RT-qPCR; fig. S1A) confirmed that the top six genes $\{-\log_{10}[P \text{ value}] > 2$ and $\log_2[\text{fold change (FC)}] < -1\}$ including *TES*, *PHF8*, *FRG1*, *GRIPAP1*, *LIN28A*, and *N6AMT1* were significantly down-regulated in the cells with reduced fatty acid. Knockdown either one of these six genes using small interfering RNAs (siRNAs) could reduce the lipid deposition in 786-O cells revealed by BIODIPY 493/503 staining (Fig. 1C and fig. S1, B and C). Of note, silencing *PHF8* resulted in the biggest decrease of lipid deposition. This finding suggested that PHF8 might be the most important determinant for lipid deposition and prompted us to further investigate the role of PHF8 in lipid deposition in ccRCC. The 786-O and 769-P cells, two VHL-null cell lines, were chosen, because both had higher levels of both PHF8 (fig. S1D) and lipid deposition (fig. S1, E and F) compared with other cell lines. We then depleted *PHF8* in 786-O and 769-P cells using sgRNA (Fig. 1D) and found that the lipid droplet formation was significantly inhibited revealed by both oil red O (ORO) staining (Fig. 1, E and F) and Triglyceride-Glo assay (Fig. 1G). We have also generated 11 ccRCC organoids derived from different patients (table S3) and found that organoid ccRCC02 carries a *VHL* mutation (c.232_239delAATCGCAG) with concurrent high *PHF8* expression (fig. S1, G and H). The role of PHF8 in lipid deposition was further confirmed by manipulating the levels of PHF8 in this organoid (Fig. 1H and fig. S1I). Last, we conducted lipidomic analysis with the 786-O cells transfected with either *PHF8*-sgRNA or Ctrl-sgRNA. The levels of 149 lipid compounds were significantly altered after *PHF8* knockout, and 75 (48.7%) of them were in the family of triglycerides (Fig. 1, I and J, and table S4). These results demonstrated that PHF8 is an important epigenetic regulator involving in lipid deposition in ccRCC.

PHF8 is essential for lipid deposition in VHL-deficient ccRCC

Multiple lines of evidence indicate that VHL/HIF axis plays a crucial role in the initiation and development of ccRCC. Consistent with more recent findings, results from our preliminary study revealed that *VHL* reexpression (Re*VHL*) in 786-O cells led to decreased lipid droplet formation (Fig. 2A and fig. S2A), substantiating the hypothesis that VHL deficiency is associated with lipid deposition in ccRCC (*10*). Because the VHL/HIF axis is involved in the regulation of JmjC-containing epigenetic regulators (*20*, *21*), we detected 21 JmjC-containing epigenetic regulators and found that seven of them were down-regulated significantly (mRNA FC [Re*VHL*/EV] < 0.5) after Re*VHL* in 786-O cells (Fig. 2B and fig. S2B). When we knocked down these seven genes including *JHDM1A*, *JHNDM2A*, *JARID1A*, *JARD1C*, *UTX*, *PHF8*, and *PHF2* (fig. S2C), PHF8 is found to be the key JmjC-containing epigenetic regulator involved in lipid deposition of ccRCC, revealed by flow cytometry using the BODIPY 493/503 probe (Fig. 2C). Overexpression of *PHF8* in 786-O Re*VHL* cells reversed Re*VHL*-induced reduction of lipid deposition (Fig. 2D and fig. S2D), suggesting that PHF8 is essential for VHL deficiency–induced lipid deposition. Furthermore, we found that the levels of PHF8, HIF1α, and HIF2α were all down-regulated by reexpressed *VHL* in VHL-null 786-O cells (Fig. 2E). Silencing either *HIF1A* or *HIF2A* resulted in down-regulation of the mRNA levels of *PHF8*, as well as their corresponding target genes, while overexpression either *HIF1A* or *HIF2A* led to the opposite effects (fig. S2, E and F), indicating that HIF1α and HIF2α play important role in PHF8 up-regulation in ccRCC. Furthermore, chromatin immunoprecipitation (ChIP)–qPCR results demonstrated that besides their well-known downstream genes, both HIF1α and HIF2α were recruited to the promoter of *PHF8* (Fig. 2, F and G), and luciferase reporter assay showed that overexpressed HIF1α and HIF2α can enhance PHF8 transcription (Fig. 2H). In addition, the mRNA and protein levels of PHF8 (Fig. 2, I and J, and fig. S2G), as well as lipid deposition (Fig. 2K), can be rescued by overexpression of the undegradable HIF1α ($HIF1A^{P402A/P564A}$, mut*HIF1A*) and HIF2α ($HIF2A^{P405A/P531A}$, mut*HIF2A*) in 786-O Re*VHL* cells. These data suggest that VHL-regulated PHF8 is HIF1α and HIF2α dependent and PHF8 is essential for lipid deposition in *VHL*-deficient ccRCC.

PHF8 promotes ccRCC tumor growth and lipid deposition in a demethylation-dependent manner

Previous studies have shown that lipid deposition can promote tumor growth by maintaining endoplasmic reticulum integrity (*32*) and cell membrane fluidity (*33*) as well as activating fatty acid receptors and subsequent downstream signaling cascade (*34*, *35*). By interfering lipid synthesis using siRNA targeting fatty acid synthase (*FASN*; fig. S3A), we found that reduction in lipid deposition led to compromised ccRCC cell proliferation (fig. S3, B and C). Moreover, knockdown of *FASN* in PHF8-overexpressed cells repressed both PHF8-induced lipid deposition and cell proliferation (fig. S3, D to F). Therefore, lipid deposition is closely associated with PHF8-induced ccRCC tumor growth. Given that PHF8 is a well-established histone demethylase, we then investigated its effect on lipid deposition and tumor growth through epigenetic regulation. We depleted *PHF8* in 786-O and 769-P cells using sgRNA and found that both cell viability and proliferation reduced greatly (Fig. 3, A to D). *PHF8* silencing in the cells derived from organoid ccRCC02 also impaired the formation of organoid (Fig. 3E). We then reintroduced either the wild-type (WT) or catalytically inactive mutant (H283A for NP_001171825.1) PHF8 to the 786-O cells transfected *PHF8*-sgRNA and found that only the WT PHF8 but not mutant PHF8 can demethylate H3K9me2/1 (Fig. 3F) and able

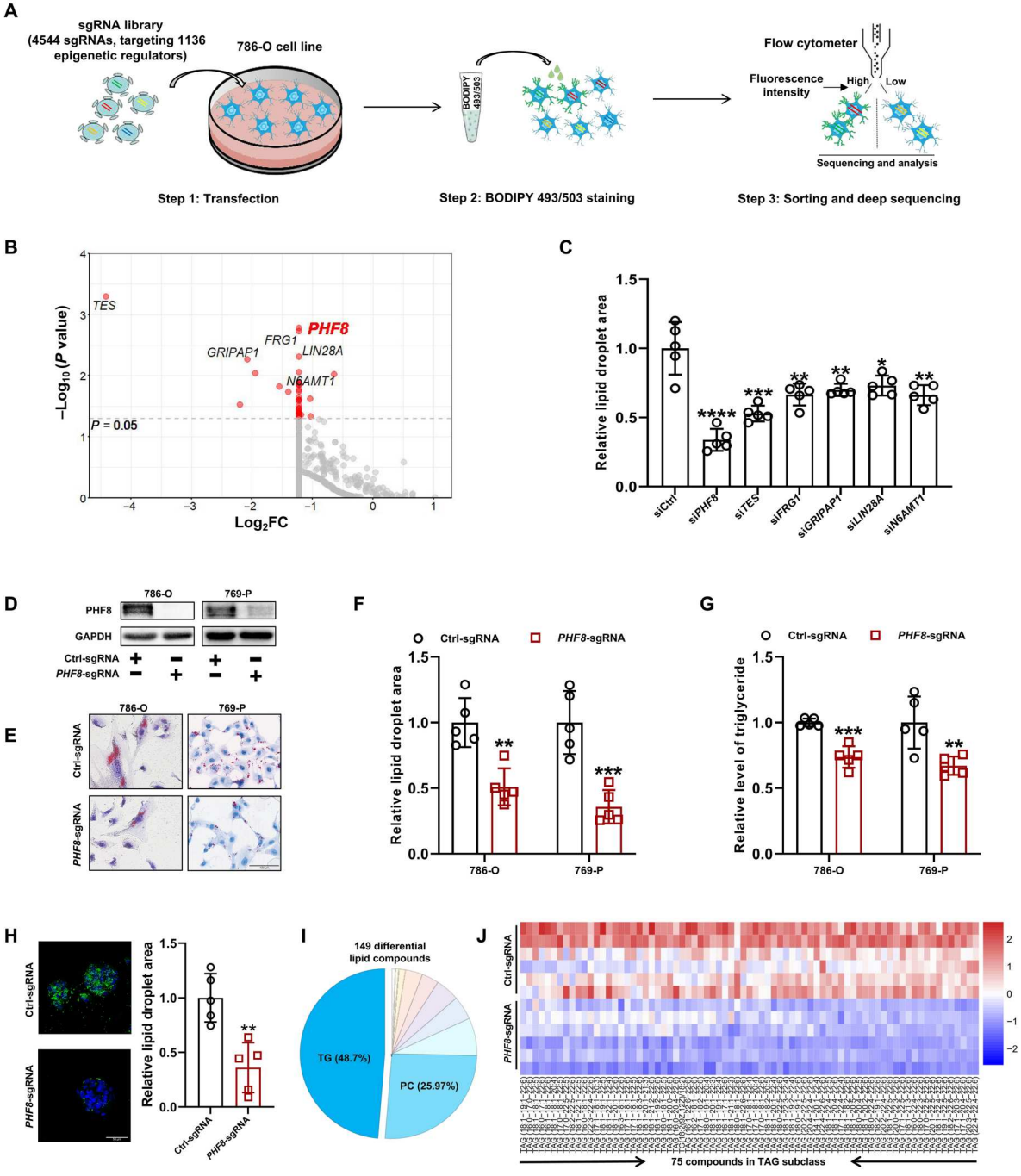

Fig. 1. A CRIPSR-Cas9 screen reveals a key role of PHF8 in the lipid deposition of ccRCC. (**A**) Scheme of CRISPR-Cas9–based epigenetic library screening to identify the determinant of lipid deposition of 786-O cells. (**B**) Volcano plot showing the genes with significantly increased small guide RNA (sgRNA) frequencies in low fatty acid group with criteria of $\log_2$[fold change (FC)] < −1 and $-\log_{10}$(*P* value) > 2. (**C**) Quantification data of lipid using BODIPY 493/503 staining in 786-O cells transfected with small interfering RNAs (siRNAs) targeting indicated genes, with scrambled siRNA as control. (**D**) Western blotting (WB) assay showing the efficiency of plant homeodomain finger protein 8 (PHF8) depletion using CRISPR-Cas9 method in 786-O and 769-P cell lines. GAPDH, glyceraldehyde-3-phosphate dehydrogenase. (**E** and **F**) Representative images (E) and quantification data (F) of lipid droplets stained with oil red O (ORO; red) in clear cell renal cell carcinoma (ccRCC) cells (786-O and 769-P) transfected with control (Ctrl)–sgRNA and *PHF8*-sgRNA. Nuclei were stained with Mayer's hematoxylin (scale bar, 100 μm in 400×). (**G**) Relative intracellular triglyceride (TG) levels revealed by using Triglyceride-Glo assay in 786-O and 769-P cell lines transfected with Ctrl-sgRNA and *PHF8*-sgRNA. (**H**) Representative fluorescence images of lipid droplets stained with BODIPY 493/503 (green) and corresponding quantification in ccRCC02 organoids transfected with *PHF8*-sgRNA or Ctrl-sgRNA. Nuclei were stained with DAPI (4′,6-diamidino-2-phenylindole; blue; scale bar, 50 μm in 400×). (**I**) Pie chart illustrating the lipid subclasses of the significantly altered lipid compounds after depleting PHF8 in 786-O cells revealed by lipomics. PC, phosphatidylcholine. (**J**) Heatmap showing that 75 identified lipid compounds belonging to TAG (triacylglycerol) subclass were decreased after PHF8 depletion in 786-O cells ($n = 6$). In (C) and (F) to (H), data are presented as means ± SD from at least three independent experiments or biological replicates, and two-tailed Student's *t* test was used. **P* < 0.05; ***P* < 0.01; ****P* < 0.001; *****P* < 0.0001.

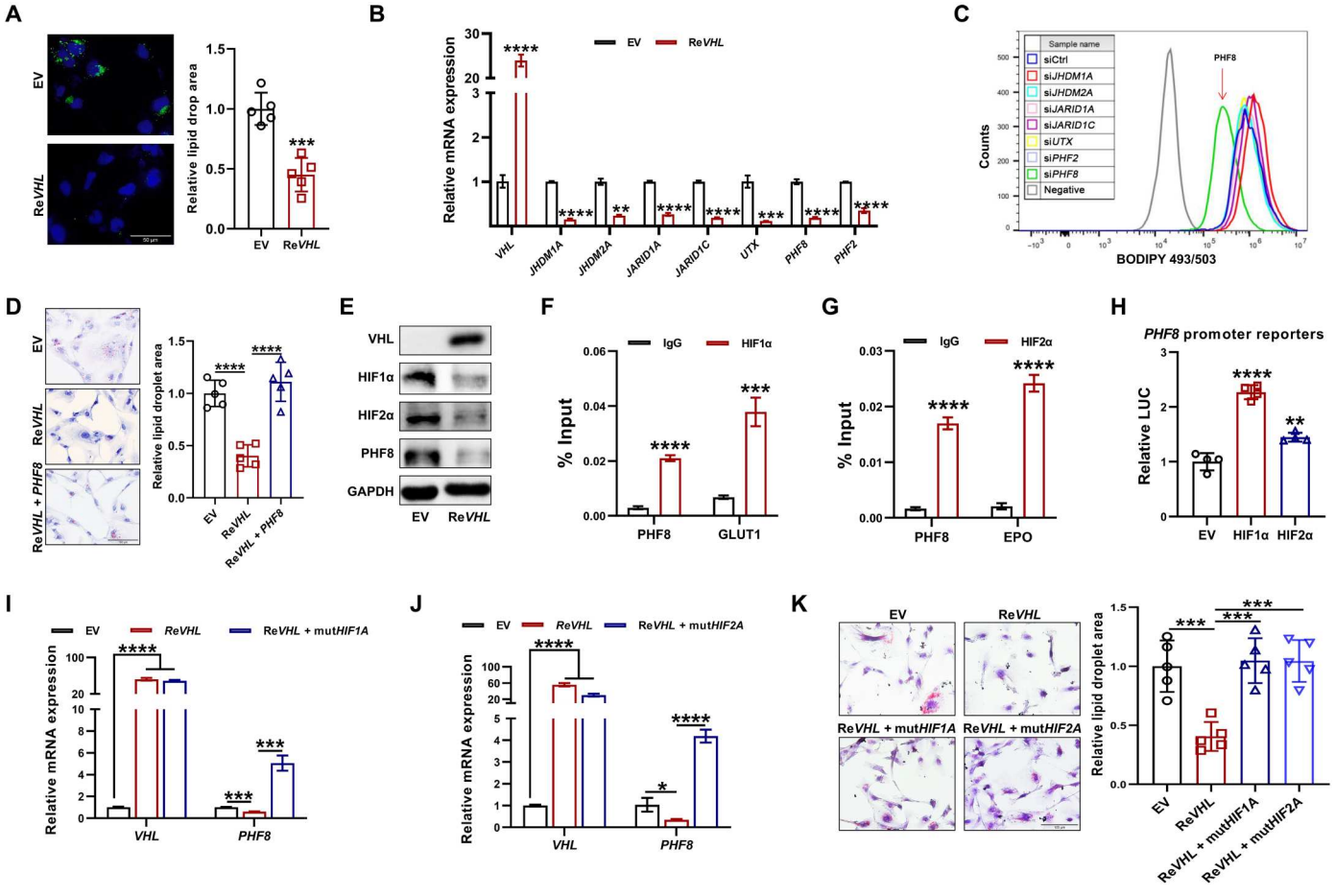

Fig. 2. PHF8 is essential for *VHL* deficiency–induced lipid deposition of ccRCC. (**A**) Representative images and quantification data of lipid droplets stained with BODIPY 493/503 (green) in 786-O with or without *VHL* reexpression (Re*VHL*). Nuclei were stained with DAPI (blue; scale bar, 50 μm). EV, empty vector. (**B**) Real-time quantitative polymerase chain reaction (RT-qPCR) analysis of relative mRNA expressions of seven JmjC-containing epigenetic regulators in 786-O with or without Re*VHL*. (**C**) Flow cytometric analysis of lipid droplets in 786-O cells transfected with siRNAs targeting indicated genes using BODIPY 493/503. (**D**) Representative images and quantification data of lipid droplets stained with ORO (red) in indicated 786-O cells. Nuclei stained with Mayer's hematoxylin (scale bar, 100 μm in 400×). (**E**) WB analysis of the indicated proteins in 786-O cells with or without Re*VHL*. (**F**) Chromatin immunoprecipitation (ChIP)–qPCR analysis of hypoxia-inducible factor 1α (HIF1α) binding on the promoter regions of *PHF8* and *GLUT1*. IgG, immunoglobulin G. (**G**) ChIP-qPCR analysis of HIF2α binding on the promoter regions of *PHF8* and *EPO*. (**H**) *PHF8* promoter–driven luciferase reporters and luciferase activity (LUC) in 786-O cells with overexpressed HIF1α and HIF2α. (**I** and **J**) RT-qPCR analysis of relative mRNA expressions of indicated genes in 786-O Re*VHL* cells with or without overexpression of nondegradable mut*HIF1A* (P402A/P564A) (I) or mut*HIF2A* (P405A/P531A) (J). (**K**) Representative images and quantification data of lipid droplets stained with ORO (red) in indicated 786-O cells. Nuclei stained with Mayer's hematoxylin (scale bar, 100 μm in 400×). In (A), (B), (D), and (F) to (K), data are presented as means ± SD from at least three independent experiments or biological replicates. Two-tailed Student's *t* test was used for (A), (B), and (F) to (H), and ordinary one-way analysis of variance (ANOVA) was used for (D) and (I) to (K). **P* < 0.05; ***P* < 0.01; ****P* < 0.001; *****P* < 0.0001.

to rescue cell viability and proliferation (Fig. 3, G and H) as well as the in vivo phenotype (Fig. 3, I and J) evidenced by the intensity of Ki67 staining (Fig. 3, K and L). In addition, the WT PHF8 but not mutant PHF8 can rescue the lipid droplet formation induced by PHF8 knockout in 786-O cells in vitro (fig. S3G) and 786-O cell–derived xenografts in vivo (fig. S3H). Together, these results demonstrated the essentiality of PHF8's demethylase activity in promoting ccRCC tumor growth and lipid deposition.

PHF8-GLUL axis plays an essential role in ccRCC tumor growth and lipid deposition

To further investigate the underlying molecular mechanism in PHF8-mediated ccRCC tumor growth and lipid accumulation, RNA sequencing (RNA-seq) was conducted, and 3575 differentially expressed genes were identified when *PHF8* is knocked out in 786-O cells (triplicates per group; data are deposited in GSE214183). Results from Kyoto Encyclopedia of Genes and Genomes (KEGG) pathway analysis showed that 26.3% of differentially expressed genes were metabolism related (Fig. 4A) in accordance with the important role of PHF8 in lipid metabolism. Of note, metabolic pathways involving alanine, aspartate, and glutamate were the most markedly affected (Fig. 4B), and this notion is further confirmed by RT-qPCR (fig. S4A). Among the differentially expressed genes, *GLUL*, encoding an enzyme responsible for glutamine de novo synthesis, is affected most severely ($\log_2$FC = −10.98) at both mRNA (Fig. 4C) and protein (Fig. 4D). In line with that GLUL-mediated glutamine synthesis is important for tumor cell proliferation (*16*, *18*), we found that silencing *GLUL* in 786-O and 769-P cells not

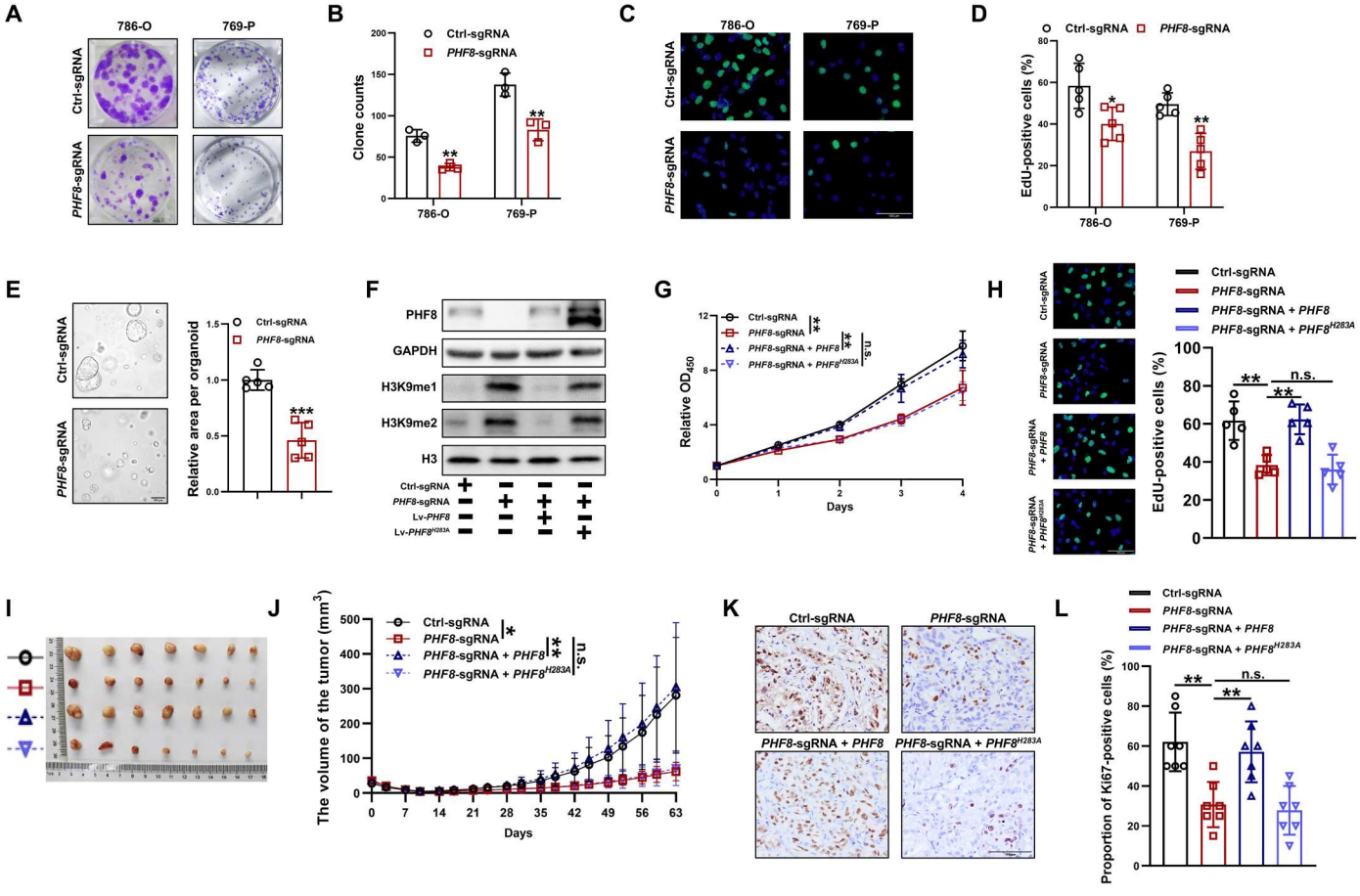

Fig. 3. PHF8 promotes ccRCC tumor growth in a demethylation-dependent manner. (**A** and **B**) Representative images (A) and quantification data (B) of colony formation assay of ccRCC cell lines (786-O and 769-P) transfected with *PHF8*-sgRNA or Ctrl-sgRNA. (**C** and **D**) Representative images (C) and quantification data (D) of 5-ethynyl-2′-deoxyuridine (EdU; green) assay of ccRCC cell lines (786-O and 769-P) transfected with *PHF8*-sgRNA or Ctrl-sgRNA. Nuclei were stained by DAPI (blue; scale bar, 100 μm in 400×). (**E**) Representative images and quantification data of organoids transfected with *PHF8*-sgRNA or Ctrl-sgRNA (scale bar, 100 μm in 200×). (**F**) WB analysis of indicated proteins in 786-O cells transfected with Ctrl-sgRNA, *PHF8*-sgRNA with or without wild-type (WT) *PHF8*, or $PHF8^{H283A}$ overexpression. (**G**) Relative optical density at 450 nm (OD_{450}) values of indicated 786-O cells detected by cell counting kit-8 (CCK-8) assay. n.s., not significant. (**H**) Representative images and quantification data of EdU (green) assay of indicated 786-O cells. Nuclei were stained by DAPI (blue; scale bar, 100 μm in 400×). (**I** and **J**) Images (I) and tumor volumes (J) of indicated 786-O cell–derived xenograft tumors ($n = 7$ per group). (**K** and **L**) Representative images (K) and quantification data (L) for immunohistochemical (IHC) staining of Ki67 in indicated 786-O cell–derived xenograft (scale bar, 100 μm in 400×). In (B), (D), (E), (G), (H), (J), and (L), data are presented as means ± SD from at least three independent experiments or biological replicates. Two-tailed Student's *t* test was used for (B), (D), and (E), and ordinary one-way ANOVA test was used for (G), (H), (J), and (L). $^*P < 0.05$; $^{**}P < 0.01$; $^{***}P < 0.001$.

only reduced cell proliferation but also the levels of glutamine (fig. S4, B to D). Reintroduced GLUL in PHF8-depleted 786-O and 769-P cells (Fig. 4D) is capable of rescuing glutamine and lipid deposition (fig. S4, E to H), cell proliferation in vitro (Fig. 4E), and tumor growth in vivo (Fig. 4, F and G). The restored GLUL is also capable of rescuing organoid formation and lipid deposition (Fig. 4H and fig. S4, I and J). In addition, acetyl-CoA acetyltransferase 2 and enoyl-CoA delta isomerase 1, two enzymes responsible for lipolysis, were up-regulated when PHF8 is knocked out (fig. S4, K and L). Because PHF8 is also recruited to their promoter (fig. S4M), PHF8 likely plays some role in lipolysis by acting as a co-repressor as reported previously (*36*). However, results of carbon flux by labeling $^{13}C_5$ glutamate substantiated that reductive carboxylation signaling is decreased in GLUL knockdown cells, evidenced by that m+5 α-ketoglutarate and m+5 citrate, two important intermediate metabolites in reductive carboxylation signaling, were lower when GLUL was silenced (fig. S4N and table S5). Given the essential roles of reductive carboxylation signaling in fatty acid synthesis in ccRCC (*8*, *14*), these results together indicated that GLUL plays an indispensable role in PHF8-regulated ccRCC tumor growth and lipid deposition.

PHF8 up-regulates GLUL by transcriptional up-regulating TEAD1

Consistent with the RNA-seq data, PHF8 knockout led to reduced mRNA levels of *GLUL* in both 786-O and 769-P cells (figs. S4A and S5A), suggesting that PHF8 may up-regulate GLUL transcriptionally. However, ChIP-qPCR and ChIP sequencing (ChIP-seq; data are deposited in GSE217161) failed to show the binding of PHF8 on the promoter region of *GLUL*, suggesting that PHF8 likely regulates GLUL indirectly (fig. S5, B and C). By conducting KEGG pathway enrichment analysis using gene set enrichment analysis

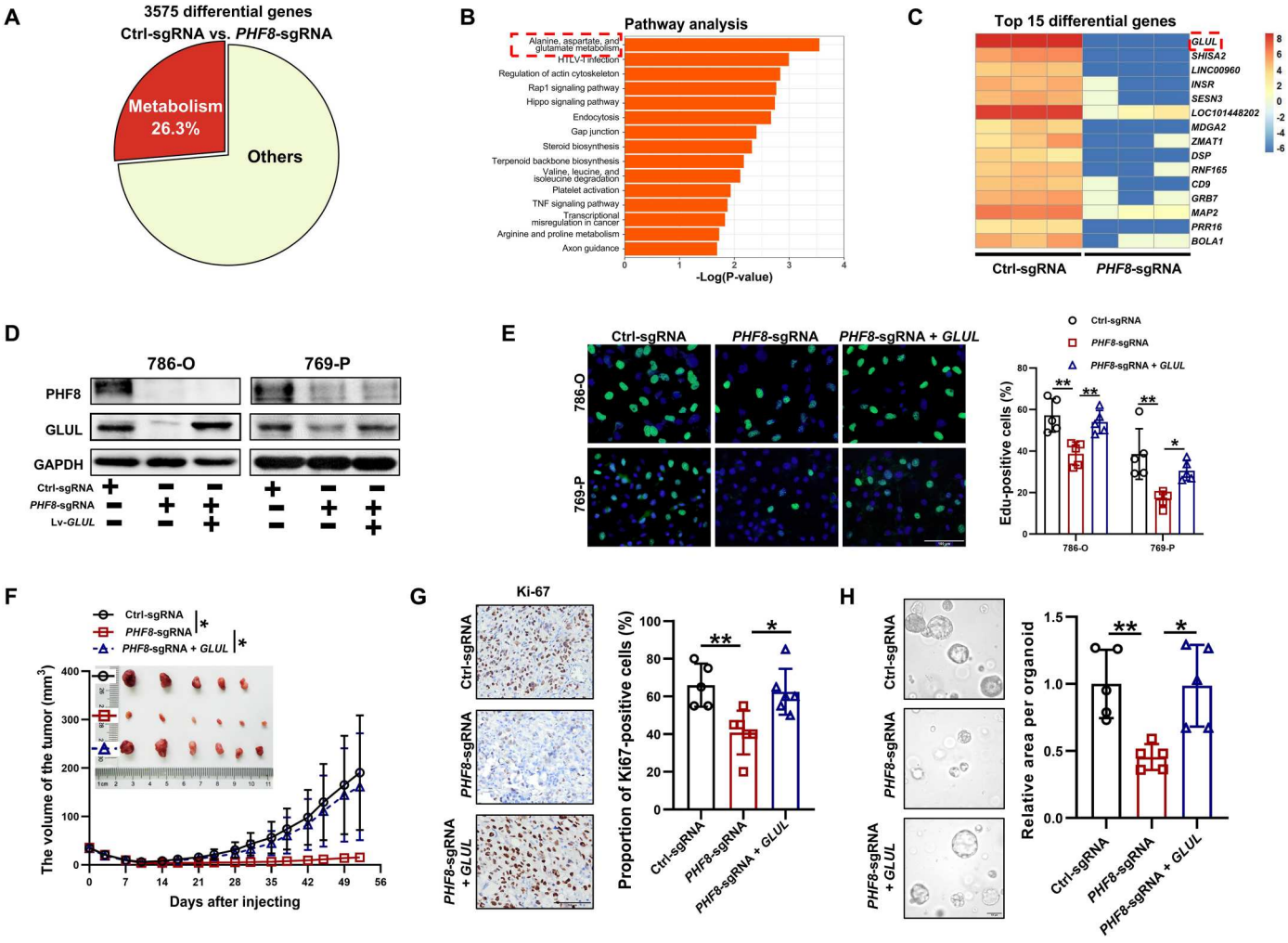

Fig. 4. GLUL expression is controlled by PHF8 and is essential for ccRCC cell proliferation. (**A**) Pie chart showing the metabolism-related gene clusters of the differential genes using Kyoto Encyclopedia of Genes and Genomes (KEGG) method based on RNA sequencing (RNA-seq) after depleting *PHF8* in 786-O cells. (**B**) Histogram showing the top 15 significantly enriched pathways using KEGG method. TNF, tumor necrosis factor. (**C**) Heatmap showing the top 15 differential genes. (**D**) WB analysis of indicated proteins in 786-O and 769-P cells transfected with Ctrl-sgRNA and *PHF8*-sgRNA with or without glutamate-ammonia ligase (*GLUL*) overexpression. (**E**) Representative images and quantification data of EdU (green) assay of ccRCC cell lines (786-O and 769-P) transfected with Ctrl-sgRNA and *PHF8*-sgRNA with or without *GLUL* overexpression. Nuclei were stained by DAPI (blue; scale bar, 100 μm in 400×). (**F**) Images and tumor volumes of indicated 786-O cell–derived xenograft tumors ($n = 5$ in Ctrl-sgRNA group and $n = 6$ in both of *PHF8*-sgRNA and *PHF8*-sgRNA + *GLUL* groups). (**G**) Representative images and quantification data for IHC staining of Ki67 in indicated 786-O cell–derived xenografts (scale bar, 100 μm in 400×). (**H**) Representative images and quantification data of organoids transfected with Ctrl-sgRNA and *PHF8*-sgRNA with or without *GLUL* overexpression (scale bar, 100 μm in 200×). In (E) to (H), data are presented as means ± SD from at least three independent experiments or biological replicates, and ordinary one-way ANOVA test was used. *$P < 0.05$; **$P < 0.01$.

(GSEA), we found that the hippo signaling pathway is most severely affected by PHF8 knockout (Fig. 5A), which is further validated by GSEA analysis (enrichment score = −0.63, adjust $P = 0.0155$; Fig. 5B). It has been reported that Yes1 associated transcriptional regulator (YAP1)/transcriptional coactivator with PDZ-binding motif/TEAD complex could regulate GLUL transcription by binding to its promoter (*37*). We performed ChIP-qPCR and dual luciferase reporter assays (fig. S5, D and E) and confirmed that YAP1 occupies *GLUL* promoter and regulates its expression. Results from the RNA-seq data indicate that most of the genes in hippo signaling pathway including *YAP1*, *TEAD1*, *TEAD2*, *TEAD3*, *CYR61*, and *CTGF* were down-regulated in the absence of PHF8 (fig. S5F). We then focused on TEAD1, because (i) reduced mRNA and protein levels of TEAD1 were consistently observed when PHF8 is knocked out (Fig. 5C and fig. S5, F and G) and (ii) high copy number of *TEAD1* is associated with worse ccRCC prognoses (Fig. 5C). Results from ChIP-seq targeting TEAD1 (ENCODE database, www.encodeproject.org) suggested that TEAD1 is enriched at the genomic loci of *GLUL* promoter (fig. S5H). We conducted ChIP-qPCR and dual luciferase reporter assays to verify the recruitment of TEAD1 to the *GLUL* promoter (fig. S5, D and E). Moreover, reexpressed PHF8 in *PHF8*-sgRNA cells enhanced the recruitment of TEAD1 to the *GLUL* promoter (fig. S5I). In addition, overexpressed TEAD1 can up-regulate the mRNA (Fig. 5D) and protein (Fig. 5E) levels of GLUL in 786-O *PHF8*-sgRNA cells. Similar results were obtained when TEAD1 is

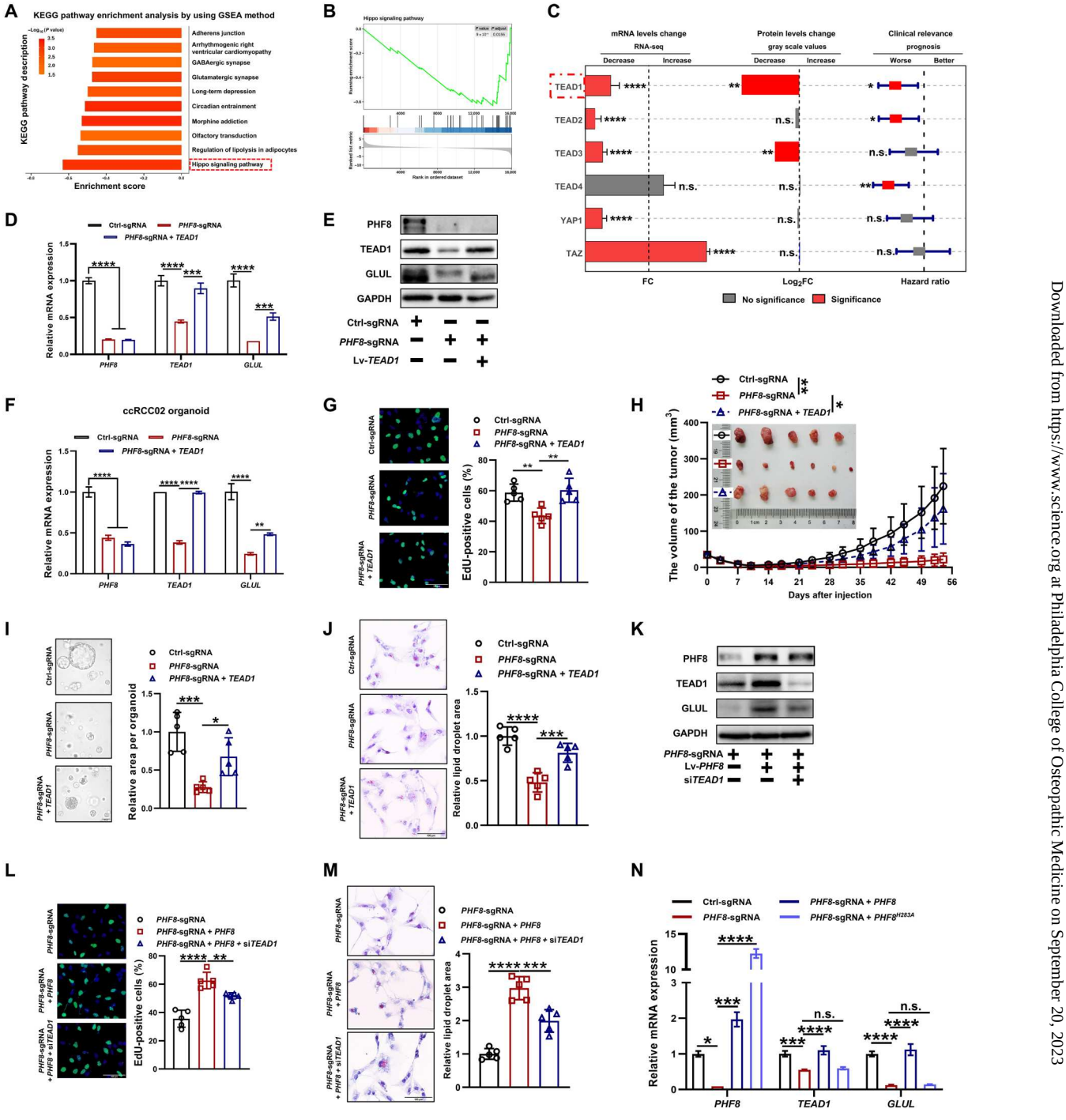

Fig. 5. The regulatory effect of PHF8 on GLUL depends on TEAD1. (**A**) Histogram showing the top 10 enriched pathways based on RNA-seq. (**B**) Gene set enrichment analysis (GSEA) enrichment plot of the hippo signaling pathway. (**C**) Integration of mRNA (RNA-seq) and protein changes after PHF8 knockout and the prognosis in ccRCC. The prognosis was evaluated by analyzing the association of copy number segments of indicated genes with survival data from The Cancer Genome Atlas. (**D**) RT-qPCR analysis of indicated genes in indicated 786-O cells. (**E**) WB analysis of indicated proteins in indicated 786-O cells. (**F**) RT-qPCR analysis of indicated genes in organoids transfected with indicated lentivirus. (**G**) EdU (green) assay of indicated 786-O cells. Nuclei were stained by DAPI (blue; scale bar, 100 μm in 400×). (**H**) Images and tumor volumes of indicated 786-O cell–derived xenograft tumors ($n = 5$ in both of Ctrl-sgRNA and *PHF8*-sgRNA + *TEAD1* groups and $n = 6$ in *PHF8*-sgRNA group). (**I**) Representative images and quantification data of the organoids transfected with indicated lentivirus (scale bar, 100 μm in 200×). (**J**) Representative images and quantification data of lipid droplets stained with ORO (red) in indicated cells. Nuclei stained with Mayer's hematoxylin (scale bar, 100 μm in 400×). (**K**) WB analysis of indicated proteins in indicated 786-O cells. (**L**) EdU (green) assay of indicated cells. Nuclei were stained by DAPI (blue; scale bar, 100 μm in 400×). (**M**) ORO (red) staining showing lipid droplets in indicated cells. Nuclei stained with Mayer's hematoxylin (scale bar, 100 μm in 400×). (**N**) RT-qPCR analysis of indicated genes in indicated 786-O cells. In (D), (F) to (J), and (L) to (N), data are presented as means ± SD from at least three independent experiments or biological replicates. Ordinary one-way ANOVA test was used. *$P < 0.05$; **$P < 0.01$; ***$P < 0.001$; ****$P < 0.0001$.

overexpressed in the ccRCC02 *PHF8*-sgRNA organoid (Fig. 5F). Overexpressed TEAD1 is also capable of enhancing cell proliferation, tumor growth (Fig. 5, G to I; and fig. S5, J and K), and lipid deposition (Fig. 5J). To ascertain the necessity of TEAD1 in PHF8/GLUL-mediated cell growth and lipid deposition, we reexpressed PHF8 and knocked down TEAD1 in 786-O *PHF8*-sgRNA cells and showed that down-regulating TEAD1 can repress PHF8-induced GLUL expression (Fig. 5K), cell growth, and lipid deposition evidenced by results from 5-ethynyl-2′-deoxyuridine (EdU; Fig. 5L) and ORO staining (Fig. 5M). Moreover, overexpressed GLUL in TEAD1 knockdown 786-O cells is capable of restoring lipid deposition and cell proliferation, which further demonstrated the essentiality of GLUL in TEAD1-mediated phenotypes (fig. S5, L to N). Consistent with above-mentioned essentiality of demethylase activity, the mRNA levels of *TEAD1* and *GLUL* can only be rescued by WT PHF8 but not the mutant PHF8 (Fig. 5N). These results suggested that PHF8 up-regulates GLUL by transcriptionally up-regulating TEAD1 in a demethylase-dependent manner.

PHF8 is recruited by c-MYC to up-regulate TEAD1

On the basis that (i) both c-MYC and PHF8 play important roles in metabolism (*38*), (ii) PHF8 can form a complex with c-MYC (*26*), and (iii) altered signature of c-MYC ($P = 0.0149$) was found after PHF8 knockout in 786-O cells when GSEA analysis was conducted with "HALLMARK_MYC_TARGETS_V2" gene set (Fig. 6A), we examined whether PHF8 regulates TEAD1 through the PHF8/c-MYC complex. Endogenously expressed PHF8 and c-MYC form a complex in both 786-O and 769-P cells (Fig. 6B and fig. S6A). However, the interaction between PHF8 and c-MYC did not require its demethylase activity evidenced by that both WT and mutant PHF8 complexed with c-MYC in human embryonic kidney 293T (HEK293T) cells (Fig. 6C and fig. S6B). Moreover, down-regulated mRNA and protein levels of TEAD1 were observed when c-MYC was silenced (fig. S6, C and D). Consistently, c-MYC overexpression can regulate the mRNA levels of *TEAD1* (fig. S6E). Results from ChIP-seq in 786-O cells (data are deposited in GSE217161) showed that ~71% of c-MYC binding sites overlap with that of PHF8 ($P = 0.0012$; Fig. 6D and fig. S6F) and metagene plot analyses showed highly overlapped chromatin-binding profiles around the transcriptional start sites (TSSs) between PHF8 and c-MYC (Fig. 6E). In addition, Fig. 6F shows that PHF8 and c-MYC co-occupy the *TEAD1* promoter region. Results from ChIP-qPCR indicate that both PHF8 and c-MYC were enriched on the *TEAD1* promoter (Fig. 6G). Because knockdown of c-MYC reduced PHF8 enrichment on the *TEAD1* promoter (Fig. 6H) and PHF8 knockout did not affect c-MYC enrichment (Fig. 6I), although silencing either of them reduced RNA–polymerase II (pol II) enrichment on *TEAD1* promoter, we conclude that PHF8 is recruited to the *TEAD1* promoter by c-MYC. This conclusion is further substantiated by analyzing the PHF8 ChIP-seq in c-MYC knockdown cells and c-MYC ChIP-seq in PHF8-sgRNA cells. The enrichment of PHF8 at genomic loci including *TEAD1* promoter declined markedly when c-MYC is knocked down (Fig. 6, F and J), while the enrichment of c-MYC remained unchanged when PHF8 is knocked out (Fig. 6, F and K). Of note, the levels of H3K9me1 and H3K9me2 on *TEAD1* promoter increased significantly when PHF8 is knocked down (Fig. 6I). The results from *TEAD1* promoter–driven luciferase assays demonstrated that TEAD1 is under the control of both PHF8 and c-MYC (Fig. 6L) and that the demethylase activity of PHF8 is indispensable for its regulation (Fig. 6M). These results indicate that PHF8, recruited to the *TEAD1* promoter by c-MYC, up-regulates TEAD1 through epigenetic modification.

The PHF8/TEAD1/GLUL axis is clinically relevant in ccRCC

To evaluate the clinical significance of PHF8/TEAD1/GLUL axis, we compared the mRNA level of *PHF8* and protein levels of PHF8, TEAD1, and GLUL in tumor and their adjacent normal tissues by RT-qPCR and Western blotting (WB), respectively (Fig. 7, A to C), and found that all of them are higher in tumor tissues. In addition, immunohistochemical (IHC) staining (Fig. 7D) revealed that the levels of PHF8, TEAD1, and GLUL are not only positively correlated with each other (Fig. 7E) but also highly associated with both higher Fuhrman grade (Fig. 7F) and poorer prognosis (Fig. 7G). These findings were further substantiated by the results from analyzing the public datasets. The mRNA levels of *GLUL* and *TEAD1* are positively correlated with that of *PHF8* (fig. S7A). The levels of PHF8, GLUL, and TEAD1 are higher in tumor tissues when proteomic data from Clinical Proteomic Tumor Analysis Consortium (http://ualcan.path.uab.edu/index.html) (*39*) were analyzed (fig. S7, B to D). Higher copy number segments of *GLUL* and *TEAD1* correlates with shorter survival (fig. S7, E and F; https://xena.ucsc.edu/kaplan-survival-analysis/). These data imply the clinical importance of PHF8/TEAD1/GLUL axis in ccRCC prognosis.

Targeting GLUL is an efficacious therapeutic strategy against ccRCC

To test whether GLUL can serve as a potential therapeutic target for ccRCC, we examined the effect of an irreversible selective GLUL inhibitor L-methionine sulfoximine (MSO) on cell proliferation. The 786-O and 769-P cells transfected with either control (Ctrl)–sgRNA or *PHF8*-sgRNA were treated with MSO in glutamine-free medium as reported previously (*16*). The cell proliferation was inhibited significantly by MSO only when PHF8 is intact but not silenced (Fig. 8, A and B, and fig. S8A). The size of the tumors (Fig. 8C) and the number of Ki67-positive cells in the tumor (Fig. 8D) derived from the 786-O xenograft reduced significantly by MSO treatment. However, these effects disappeared when PHF8 is silenced. Similar findings were obtained when the organoids were treated with MSO (Fig. 8E). Consistent with previous studies (*40*, *41*), we found that GLUL inhibition also activated the mechanistic target of rapamycin kinase (mTOR) signaling pathway in 786-O cells (Fig. 8F). We hypothesized that MSO may function synergistically with the mTOR signaling pathway inhibitor EVE, a second-line drug for ccRCC. To test our hypothesis, we conducted a series of in vitro and in vivo experiments with either MSO or EVE alone or in combination. Our results showed that the number of proliferating cells (Fig. 8G and fig. S8, B and C), the size of the organoids (Fig. 8H) and 786-O–derived xenograft (Fig. 8I) or patient-derived xenografts (PDXs; Fig. 8J), as well as the number of Ki67-positive cells (Fig. 8, K and L) can be repressed by either of them alone and combination of these two drugs that functioned synergistically. In addition, MSO can inhibit lipid deposition significantly when the cells expressing intact PHF8 but not when PHF8 is silenced (fig. S8, D to G), whereas EVE cannot repress the lipid deposition (fig. S8, F and G). These data together demonstrated that MSO alone, but more

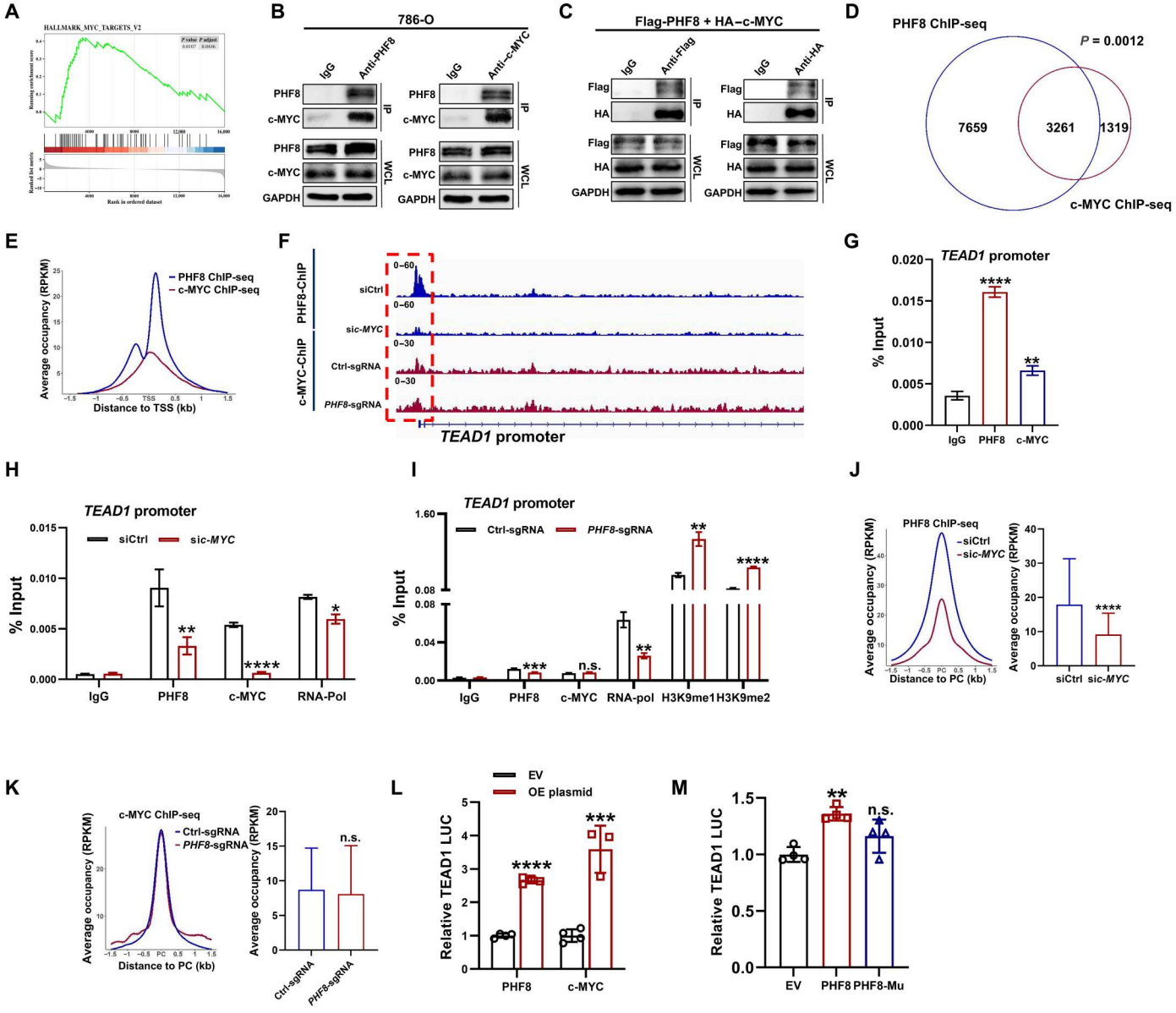

Fig. 6. PHF8 interacts with c-MYC to up-regulate TEAD1 in a demethylation-dependent manner. (**A**) GSEA enrichment plot of the HALLMMARK_MYC_TARGETS_V2 gene set based on the RNA-seq data. (**B**) WB analysis of whole-cell lysates (WCLs) and immunoprecipitates (IPs) with PHF8 and c-MYC antibodies in 786-O cells. (**C**) WB analysis of WCLs and immunoprecipitates with Flag and HA antibodies in 293T cells transfected with the indicated plasmids. (**D**) Venn diagram showing the common peaks of PHF8 and c-MYC in the ChIP-seq results. (**E**) Metagene plot of ChIP-seq profiles of PHF8 and c-MYC peaks on the transcriptional start site (TSS) region. RPKM, reads per kilobase per million mapped reads. (**F**) ChIP-seq tracks from indicated cells at the genomic loci of *TEAD1*. (**G**) ChIP-qPCR assays of PHF8 and c-MYC binding on the promoter region of *TEAD1*. (**H**) ChIP-qPCR analysis of PHF8, c-MYC, and RNA–polymerase II (Pol II) binding on the promoter region of *TEAD1* in 786-O cells transfected with siRNA targeting *c-MYC* and with scrambled siRNA as control. (**I**) ChIP-qPCR analysis of PHF8, c-MYC, RNA-Pol II, H3K9me1, and H3K9me2 binding on the promoter region of *TEAD1* in 786-O cells transfected with Ctrl-sgRNA and *PHF8*-sgRNA. (**J**) Metagene profile and bar plot of PHF8 binding in 786-O cells transfected with siRNA targeting *c-MYC* and with scrambled siRNA as control. PC, peak center. (**K**) Metagene profile and bar plot of c-MYC binding in 786-O cells transfected with or without *PHF8*-sgRNA. (**L**) *TEAD1* promoter–driven luciferase reporter assay in 786-O cells transfected with EV, WT *PHF8* or *c-MYC*. OE, overexpressed. (**M**) *TEAD1* promoter–driven luciferase reporter assay in 786-O cells transfected with EV, WT *PHF8*, or $PHF8^{H283A}$. In (G) to (M), data are presented as means ± SD from at least three independent experiments or biological replicates. Two-tailed Student's *t* test was used. **P* < 0.05; ***P* < 0.01; ****P* < 0.001; *****P* < 0.0001.

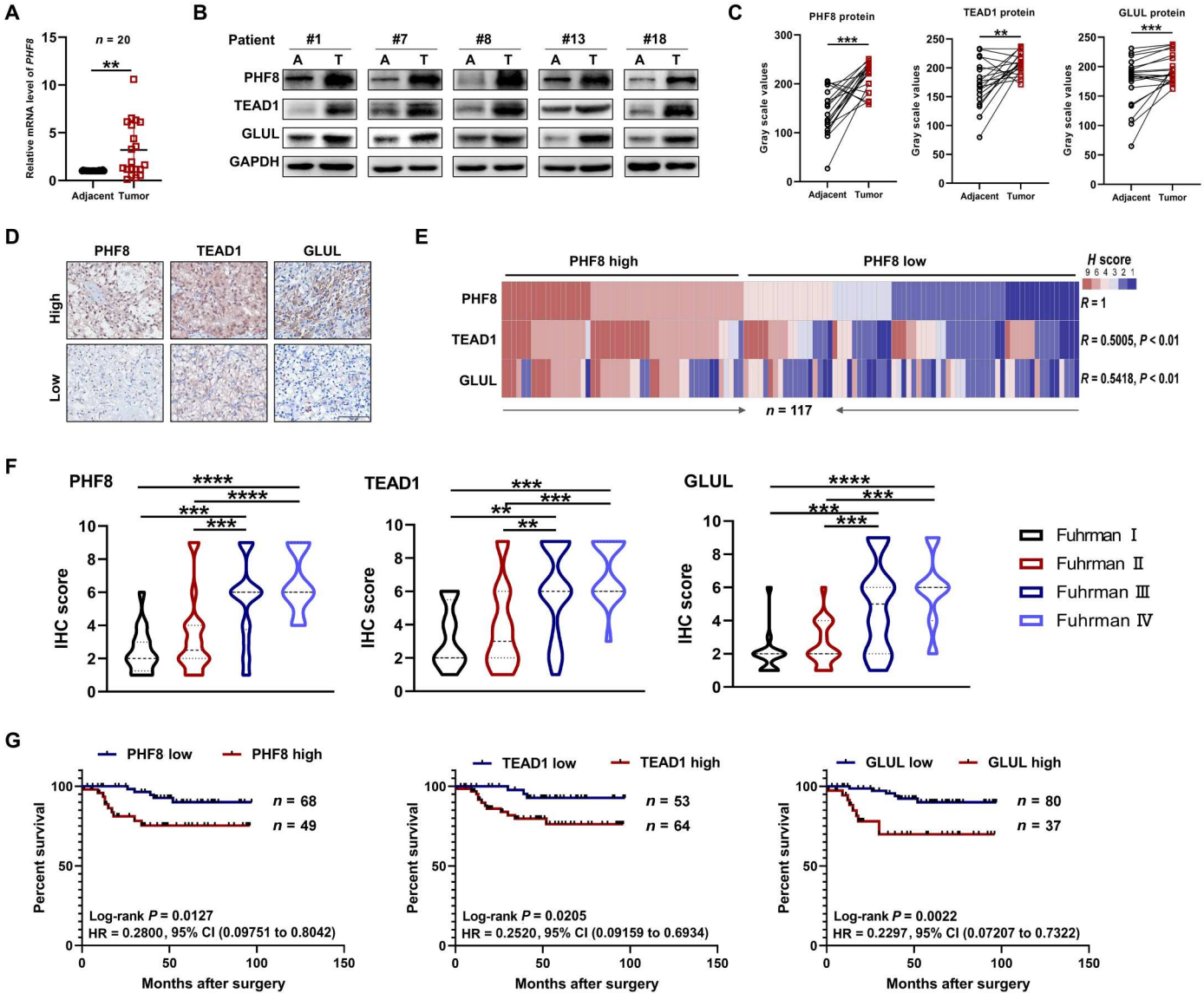

Fig. 7. PHF8/TEAD1/GLUL axis is clinically important for ccRCC progression. (**A**) RT-qPCR analysis of relative mRNA levels of *PHF8* in paired adjacent and tumor tissues ($n = 20$). (**B** and **C**) WB analysis (B) and mean gray scale values (C) of indicated proteins in paired adjacent and ccRCC tissues ($n = 20$). (**D**) Representative images for IHC staining of PHF8, TEAD1 and GLUL in our ccRCC tissue microarray (TMA; $n = 117$; scale bar, 100 μm in 400×). (**E**) Heatmap showing the *H* score of each ccRCC sample ($n = 117$) and illustrating the Spearman's correlation coefficient (*R*). (**F**) Violin plot showing that *H* score distribution between different Fuhrman grades. (**G**) Kaplan-Meier plot of survival based on the *H* score of PHF8, TEAD1, and GLUL (high group: *H* score > 4, low group: *H* score ≤ 4; $n = 117$). HR, hazard ratio; CI, confidence interval. In (A) and (C), data are presented as scatter point. In (F), data are presented using violin plots. In (G), data are presented using Kaplan-Meier plots of survival. Paired two-tailed Student's *t* test was used for (A) and (C), Kruskal-Wallis test was used for (F), log-rank test was used for (G), and Spearman's correlation analysis was used for (E). $^{**}P < 0.01$; $^{***}P < 0.001$; $^{****}P < 0.0001$.

efficiently in combination with EVE, can repress not only lipid deposition but also ccRCC progression.

DISCUSSION

In this study, we reported a previously unidentified regulatory axis involved in tumor growth and lipid deposition in ccRCC. We identified PHF8 as an important epigenetic regulator involved in VHL/HIF-mediated tumor growth and lipid deposition. Mechanistically, PHF8 interacts with c-MYC and transcriptionally activates TEAD1 in a demethylation-dependent manner. Up-regulated TEAD1 subsequently enhances GLUL transcription by binding to its promoter directly and ultimately promotes tumor growth and lipid deposition (Fig. 9). Activated PHF8/TEAD1/GLUL axis is also associated with higher Fuhrman grade and poorer prognosis of patients with ccRCC. Therapeutically, GLUL inhibitor MSO can efficiently suppress the tumor growth and lipid deposition as well as enhance the anticancer effect of EVE (Fig. 9), which provides a previously unknown avenue for ccRCC treatment.

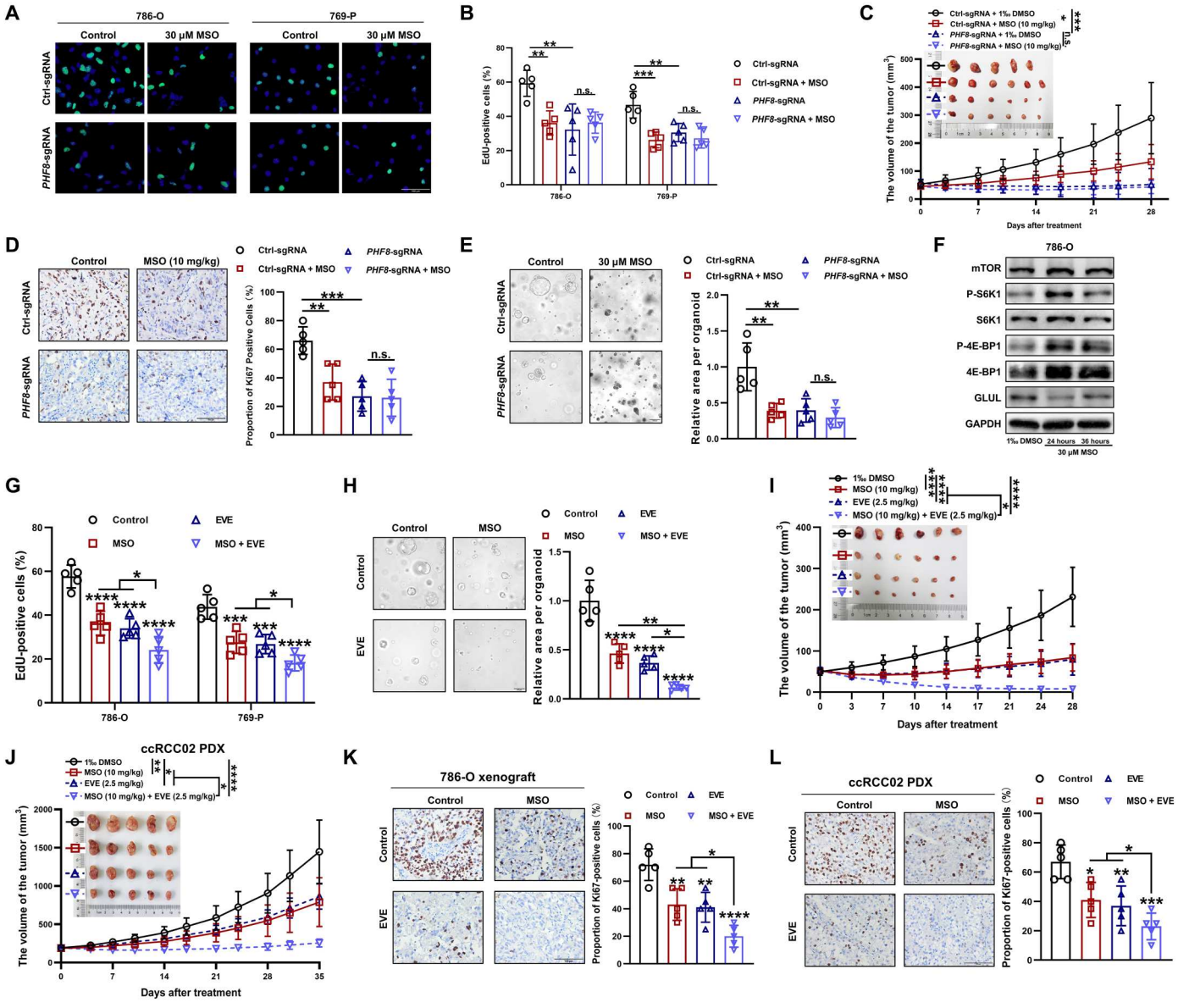

Fig. 8. GLUL inhibition suppresses ccRCC growth and enhances the anti-cancer effects of EVE. (**A** and **B**) Representative images (A) and quantification data (B) of EdU (green) assay in 786-O and 769-P cells treated with indicated regimens. Nuclei were stained by DAPI (blue; scale bar, 100 μm in 400×). (**C**) Images and tumor volumes of xenograft tumors formed by indicated 786-O cells with or without L-methionine sulfoximine (MSO) treatment ($n = 5$ in Ctrl-sgRNA group and $n = 6$ in *PHF8*-sgRNA group as well as Ctrl-sgRNA and *PHF8*-sgRNA treated with MSO groups). ‰, per mil. (**D**) Ki67 staining in indicated 786-O cell–derived xenografts with indicated treatments (scale bar, 100 μm in 400×). (**E**) Organoids transfected with Ctrl-sgRNA and *PHF8*-sgRNA treated with indicated regimens (scale bar, 100 μm in 200×). (**F**) WB analysis of the indicated proteins in 786-O cells treated with or without MSO (30 μM) for indicated time points. (**G**) Quantification data of EdU (green) assay of 786-O and 769-P cells treated with indicated regimens. EVE, everolimus. (**H**) Organoids treated with indicated regimens (scale bar, 100 μm in 200×). (**I**) Images and tumor volumes of xenograft tumors formed by 786-O cells treated with indicated regimens ($n = 6$ per group). (**J**) Images and tumor volumes of patient-derived xenografts (PDXs) treated with indicated regimens ($n = 5$ per group). (**K**) Ki67 staining in 786-O cell–derived xenografts treated with indicated regimens (scale bar, 100 μm in 400×). (**L**) Ki67 staining in PDXs treated with indicated regimens (scale bar, 100 μm in 400×). Glutamine-free medium used in (A), (B), and (E) to (H). In (B) to (E) and (G) to (L), data are presented as means ± SD from at least three independent experiments or biological replicates. Ordinary one-way ANOVA test was used. *$P < 0.05$; **$P < 0.01$; ***$P < 0.001$; ****$P < 0.0001$.

Lipid deposition plays critical roles in development, progression, and drug resistance of multiple cancers including colorectal cancer, lung cancer, breast cancer, glioblastoma, and hepatocellular carcinoma (*4*, *5*, *42*). Lipid deposition is recognized as a prominent feature and associated with malignancy, prognosis, and antiangiogenesis drug resistance in ccRCC (*3*, *9*). Qu *et al.* (*43*) found that lipid deposition could promote ccRCC cells proliferation and xenograft growth. Li *et al.* (*44*) reported that high lipid deposition contributes to metastasis of ccRCC. Lucarelli *et al.* (*45*) showed that lipid accumulation is involved in ccRCC chemotherapy resistance. However, the underlying mechanism in lipid deposition is largely unknown. Recently, aberration of VHL/HIF axis has been linked

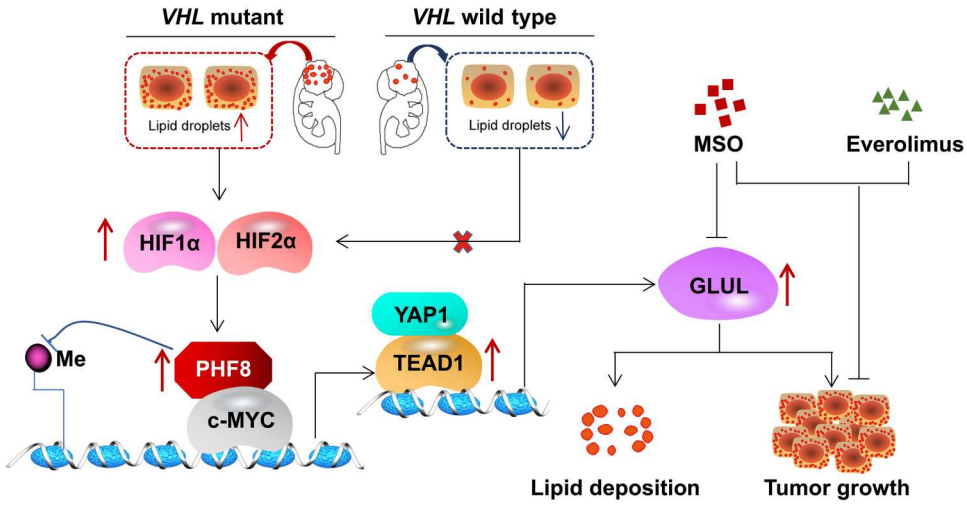

Fig. 9. Schematic illustration of the proposed model in which PHF8/TEAD1/GLUL axis regulates VHL-mediated lipid deposition and tumor growth of ccRCC.

to lipid deposition by reducing adipose triglyceride lipase–mediated lipolysis (*46*) and carnitine palmitoyl transferase 1A–regulated fatty acid β-oxidation (*10*). Given that the important role of epigenetic regulation and VHL/HIF axis in ccRCC (*19*), we explored whether epigenetic regulator is involved in VHL/HIF-mediated lipid deposition. By using unbiased CRISPR-Cas9 screening targeting 1136 epigenetic regulators, we identified the histone demethylase PHF8 as an important factor driving lipid deposition.

Glutamine is crucial for cell proliferation, pH homeostasis, and redox balance by serving as an intermediate metabolite for protein, lipid, nucleotide, and glutathione (*47*). Recently, the role of glutamine in tumorigenesis (*15*), progression (*48*), metastasis (*49*), and drug resistance (*50*) has attracted increasing attention. For the cells in solid cancers, glutamine demand could not be satisfied by the restricted availability of circulating glutamine (*17*, *51*). As a result, many tumors up-regulate GLUL to increase glutamine synthesis, especially at times of enhanced metabolic needs for high proliferation rate (*47*). Tardito *et al.* (*15*) found that tumor cells seem to prefer the endogenously synthesized glutamine over exogenous glutamine. Consistently, elevated levels of GLUL have been found in multiple cancer types with poor prognosis (*47*). In this study, we first revealed that GLUL has important roles in ccRCC growth, and its expression is correlated with the severity and poor prognosis in patients with ccRCC. Given the fact that glutamine is accumulated while glutamine utilization is increased in ccRCC (*2*, *8*), GLUL-mediated endogenously glutamine synthesis might be the reason for glutamine accumulation. Therefore, GLUL inhibitor MSO is capable of repressing both tumor growth and lipid deposition. Notably, the inhibitory effect of MSO might depend on the expression of PHF8, because MSO treatment did not further reduce proliferation when GLUL is undetectable in PHF8 knockout cells (Fig. 4D).

Hippo and MYC signaling pathways are tightly related to multiple cancers. Hippo signaling pathway plays major roles in organ size control, cell proliferation, stem cell self-renewal, tumorigenesis, and drug resistance (*52*, *53*). Accumulative evidences suggested that hippo signaling pathway promotes ccRCC development, progression, invasion, and metastasis (*54*). Carter *et al.* (*55*) found that deletion of large tumor suppressor kinase 1/2, the important regulators of the hippo signaling pathway, leads to spontaneous RCC formation in mouse. On the other hand, MYC signaling involves in a wide range of oncogenic processes including proliferation, differentiation, metastasis, and apoptosis (*56*). MYC signaling is also a well-documented pathway closely related to metabolic pathways including glutamine metabolism (*38*). In our study, we found that there is a cross-talk between the hippo and MYC oncogenic signaling. We demonstrated that PHF8, as a "bridge" of the two oncogenic pathways, is required for the regulatory function of c-MYC on TEAD1.

Although we have demonstrated that PHF8-GLUL axis plays important role in both tumor growth and lipid deposition and lipid deposition is closely related to tumor growth in ccRCC, the precise mechanism underlying how PHF8-induced lipid deposition drives ccRCC progression needs to be further investigated. Similarly, the importance of GLUL-mediated glutamine synthesis in ccRCC lipid deposition remains to be deciphered. Since GLUL can catalyze the synthesis of glutamine from TCA cycle–derived carbons (*15*), it appears paradoxical that GLUL is crucial for lipid deposition, because glutaminase (GLS)-mediated glutamine catabolism via reductive carboxylation is the key process for lipid deposition in VHL-null cells. However, because GLUL is mainly located in the cytoplasm while GLS is mainly in the mitochondria (www.proteinatlas.org) (*57*), we speculate that GLUL might be involved in transforming excess cytoplasmic glutamate into glutamine, which is then transported to the mitochondria and subsequently becomes lipid synthesis precursors via GLS-mediated reductive carboxylation. Furthermore, GLUL might affect lipid synthesis indirectly, because GLUL is also involved in the transcriptional regulation of sterol regulatory element–binding protein 1 (SREBP1), the master regulator of cholesterol and lipid syntheses (*58*). Although there could be other explanations for the important roles of GLUL in lipid deposition, the detailed mechanism underlying GLUL-involved lipid production needs to be further revealed, especially by labeling the endogenously synthesized glutamine and analyzing its subcellular localization. Further research in this field will not only better our understanding of the mechanism in GLUL-mediated lipid deposition in ccRCC but also pave the way for GLUL-related therapeutics.

MATERIALS AND METHODS

Experimental design

These experiments were designed to reveal the roles of PHF8/TEAD1/GLUL axis in the lipid deposition and tumor progression of ccRCC and investigate the therapeutic effects of MSO targeting this axis on ccRCC. First, we used an unbiased CRISPR-Cas9 screening targeting 1136 epigenetic regulators to identify that PHF8 is the determinant of lipid deposition of ccRCC. The subsequent experiments were focused on examining how PHF8 regulates the lipid deposition and tumor progression of ccRCC. Cell lines, organoids, PDX, and subcutaneous xenografts were used in this study. To investigate the underlying mechanism, we used co-IP (CoIP), ChIP-seq, ChIP-qPCR, dual luciferase reporter assay, and carbon metabolite analysis. Furthermore, we validated the important roles of this axis in ccRCC by using the data of patients with ccRCC from either our own cohort or public database. Last, we conducted a series of in vitro and in vivo experiments to demonstrate the therapeutic effect of MSO, targeting GLUL, alone, or in combination with EVE on ccRCC. The investigators were not blinded to the allocation of groups during experiments or subsequently during the analysis. Although statistical methods were not used to predetermine sample size, sample sizes were chosen on the basis of estimates from pilot experiments and previously published results. The *n* values and particular statistical methods are indicated in the figure legends and the "Statistical analysis" section.

Reagents and antibodies

MSO (M5379) was purchased from Sigma-Aldrich (St. Louis, MO, USA), EVE (S1120) was purchased from Selleck Chemicals (Houston, TX, USA), BODIPY 493/503 (D3922) was purchased from Thermo Fisher Scientific (Waltham, MA, USA). Primary antibodies used in this study are listed in table S6.

Experimental models and subject details

Cell culture

The ccRCC cell lines 786-O [the American Type Culture Collection (ATCC) number: CRL-1932], 769-P (ATCC number: CRL-1933), ACHN (ATCC number: CRL-1611), HK-2 (ATCC number: CRL-2190), and HEK293T (ATCC number: CRL-11268) were purchased from Cell Bank of Shanghai Institutes for Biological Sciences (Shanghai, China). A498 (ATCC number: HTB-44), RCC4 (European Collection of Authenticated Cell Cultures, cat. no. 03112702), and OS-RC-2 (cell number: RCB0735, RIKEN Cell Bank, Tsukuba, Japan) were provided by G. Sun (Department of Urology, West China Hospital, Sichuan University). 786-O, 769-P, and OS-RC-2 cells were maintained in RPMI 1640 (C11875500BT, Gibco, Waltham, MA, USA) containing 10% fetal bovine serum (FBS; 10099141, Gibco). RCC4, ACHN, and HEK293T cells were cultured in Dulbecco's modified Eagle's medium (DMEM; 11965118, Gibco) supplemented with 10% FBS. A498, and HK-2 cells were cultured in MEM (SH30024.01, HyClone) supplemented with 10% FBS. The cells were incubated in 5% CO_2 at 37°C. According to the manufacturer's instruction, ViaFect (E4981, Promega Corporation, Madison, WI, USA) was used for plasmids transfection, Lipofectamine 2000 (11668019, Invitrogen, Carlsbad, CA, USA) was used for siRNA transfection, and polybrene (H9268, hexadimethrine bromide, Sigma-Aldrich) was used for lentivirus transfection.

Human tissue samples

All procedures involving human participants were obeyed with the ethical standards of the institutional research committee, the 1964 Helsinki Declaration and its later amendments, or comparable ethical standards. Written informed consent was obtained from each patient. All samples were collected by Department of Urology with approval from the Research Ethics Committee of Daping Hospital, Army Military Medical University (no. 2020-67, Chongqing, China). Briefly, fresh tumor tissues and matched normal tissues from 20 patients with ccRCC were subjected to immunoblotting and RT-qPCR. Human ccRCC tissue microarray (TMA) containing a total of 117 archived paraffin-embedded specimens were subjected to IHC staining. The information of the patients was listed in table S7.

Organoids

Tumor tissues from 11 patients with ccRCC were collected to establish ccRCC organoids as described previously with some modifications (*59*, *60*). In brief, these tissues were cut into small pieces (1 to 2 mm in size), digested with type II collagenase (17101015, Gibco) for 120 min, and centrifuged at 350 g/s for 5 min at 4°C. The resuspended cells were embedded in 75% (v/v) Matrigel (Corning, NY, USA) solution and cultured with 500 μl of Advanced DMEM/F-12 (Gibco) supplemented with 5% FBS (Gibco), 1× B27 (17504044, Gibco), 10 mM Y-27632 dihydrochloride (M1817, AbMole BioScience, Houston, TX, USA), noggin (100 ng/ml), fibroblast growth factor 2 (20 ng/ml; 100-18B, PeproTech, Rocky Hill, NJ, USA), 1× ITS [insulin (5 μg/ml), transferrin (5 μg/ml), and selenium (5 ng/ml); I1884, Sigma-Aldrich], and 1× penicillin/streptomycin (15140122, Gibco) per well after Matrigel solidifying. The detailed clinical information of the patients was summarized in table S3.

Animals

All animal experiments were approved by the Institutional Animal Care and Use Committee of Army Medical University (Chongqing, China) and in accordance with international laws (European Economic Community Council Directive 86/609, O.J. L 358.1, 12 December 1987; *Guide for the Care and Use of Laboratory Animals*, U.S. National Research Council, 1996). All mice were housed in the Animal Experimental Center of Daping Hospital with a 12/12-hour light/dark cycle at 25°C and were fed with standard chow and filtered sterile water. Athymic nude mice were obtained from Vital River company (Beijing, China). NOD-Prkdc(scid)IL2rgamma(null) (NPG) mice were purchased from Vitalstar (Beijing, China). 786-O cells (5×10^6) were injected subcutaneously into the flank of 4- to 6-week-old mice. Cell-derived xenografts were measured twice per week. Tumor volumes were calculated using the formula length × width × width/2.

Patient-derived xenograft

Patients' tumor samples were cut into 1 to 2 mm pieces, and the tissue fragments were seeded under the renal capsule for tissue amplification within 4- to 6-week-old NPG mice. For passaging or drug experiments, PDXs were collect, cut into 2-mm pieces, and implanted subcutaneously into the flank region. The drug treatment and measurement were conducted in accordance with the protocol of nude mice.

Method details

Gene silencing

siRNAs targeting *PHF8*, *JARID1A*, *JARID1C*, *JHDM1A*, *JHDMA2A*, *UTX*, *PHF2*, *TEAD1*, *GLUL*, *FASN*, and *c-MYC* were purchased from RiboBio (RiboBio Co. Ltd., Guangzhou, Guangdong, China). siRNAs targeting *TES*, *FRG1*, *GRIPAP1*, *LIN28A*, and *N6AMT1* were synthesized by Sangon (Sangon Biotech, Shanghai, China). All siRNAs were used to transiently knock down the indicated genes, with scrambled siRNA as the control. In brief, cells were cultured until 70 to 80% confluence in six-well were infected with 50 nM siRNAs in presence of 5 μl of Lipofectamine 2000 (11668019, Thermo Fisher Scientific) according to the manufacturer's protocol. After 24 hours of transfection, the cells were harvested for next manipulation. To stably knock out *PHF8*, sgRNA (four sgRNAs targeting human *PHF8*) was cloned into lentiCRISPR v2 vector and then expressed in lentivirus. Cells with 70 to 80% confluence were infected by lentivirus containing sgRNAs targeting *PHF8* in presence of polybrene (8 ng/ml), and scrambled sgRNA was used as control. After 48 hours of transfection, puromycin was added to select infected cells until 5 days. Then, a monoclonal cell population was isolated by limiting dilution method. The siRNA and sgRNA sequences are listed in table S8.

Gene overexpression

The plasmids containing full-length cDNAs of *VHL*, *GLUL*, *PHF8*, and *TEAD1* were purchased from GeneCopoeia (Rockville, MD, USA). MYC-*HIF2A* was obtained from OriGene (RC208604). Hemagglutinin–*c-MYC*, *Flag-HIF1A*, *Flag-PHF8*, $HIF1A^{P402A/P564A}$, $HIF2A^{P405A/P531A}$, and $PHF8^{H283A}$ were synthesized by Sangon. For transiently overexpression, the cells with 70 to 80% confluence in six-well plate were infected with 3 μg of plasmids and 9 μl of ViaFect (Promega) for 24 hours. For stable overexpression, the plasmids were introduced into cells by lentiviral delivery in presence of polybrene (8 ng/ml). All the plasmids used were listed in table S6.

Epigenetic library screening in 786-O cells

The sgRNAs of epigenetic library that targets 1136 genes (four sgRNAs per gene; table S1) was provided by B. Wang (Department of Gastrology, Daping Hospital) and cloned into lentiCRISPR v2 vector. 786-O cells were infected with lentivirus containing pooled epigenetic sgRNA for 12 hours in the medium supplemented with polybrene (8 ng/ml). The cells were selected by puromycin (1 μg/ml) for 5 days and then harvested, fixed, and stained using BODIPY 493/503 (Thermo Fisher Scientific). The stained cells were classified into two subgroups with low or high fatty acid by flow cytometry. The sgRNA cassettes were amplified from genomic DNA using two-step PCR and deep sequencing adapters, and sample barcodes were added during the PCR. Last, sgRNA contents were measured with sequencing by GENEWIZ (Genewiz, Suzhou, China). Enrichment of sgRNAs in low fatty acid group was compared with that of high fatty acid group. Briefly, the libraries with different indices were multiplexed and loaded on an Illumina HiSeq/NovaSeq instrument according to the manufacturer's instructions (Illumina, San Diego, CA, USA). Sequencing was carried out using a 2 × 150 paired-end configuration; image analysis and base calling were conducted by the HiSeq Control Software + Off-Line Basecaller + GAPipeline-1.6 (Illumina) on the HiSeq instrument. The significantly changed genes were chosen by setting threshold at level of $P < 0.05$. The summary result was shown in table S2.

Mice treatment

MSO was dissolved in phosphate-buffered saline (PBS) and injected intraperitoneally once every 2 days (10 mg kg^{-1}). EVE was dissolved in 30% (v/v) propylene glycol, 5% (v/v) Tween 80, and 65% (v/v) ddH_2O and given by gavage daily (2.5 mg kg^{-1}). For control group, mice were treated with 1 per mil (‰) dimethyl sulfoxide by gavage daily. All xenografts were measured twice per week, and their width and length were recorded. All xenografts were harvested and further subjected to IHC staining, ORO staining, or BODIPY 493/503 staining.

RNA extraction and RT-qPCR

Total RNA was extracted using TRIzol Reagent (Jiangsu Cowin Biotech, Jiangsu, China) and purified using Ultrapure RNA Kit (CW0581M, CWBIO). First-strand cDNA was synthesized using the HiScript II Q RT SuperMix (R222-01, Vazyme, Nanjing, China) and 1 μg of purified RNA for each reaction. AceQ qPCR SYBR Green Master Mix (Q111-02, Vazyme) and primers were used for RT-qPCR. Each reaction was performed in at least triplicate. The relative mRNA expression was analyzed by using FC ($2^{-\Delta\Delta Ct}$). The primers used in our study were showed in table S8.

RNA sequencing

Total RNA was extracted from 786-O cells transfected with Ctrl-sgRNA and *PHF8*-sgRNA. After quality controlling and RNA library preparing, triplicate samples were subjected to sequence by Shanghai NovelBio Bio-Pharm Technology Co. Ltd. (Shanghai, China). RNA-seq reads were filtered and mapped to human genome (GRCh38, National Center for Biotechnology Information) using Hierarchical Indexing for Spliced Alignment of Transcripts 2 (*61*). The significance was listed by setting FCs threshold at a level of absolute value of $\log_2(FC) > 1$ and an FDR of <0.05 based on DEseq2 (*62*). The differentially expressed gene lists were subsequently analyzed using gene ontology, KEGG, or GSEA method.

ChIP PCR

The procedure of producing DNA fragments was according to the manufacturer's introduction (53009, ChIP-IT Express Enzymatic kit, Active Motif). Briefly, about 1×10^7 cells were cross-linked in 1% formaldehyde (9027, 16% formaldehyde solution, Thermo Fisher Scientific) at room temperature for 10 min, following by 5 min of blocking with 1× glycine buffer. The cells were collected and lysed with lysis buffer on ice. The nuclei were collected through centrifuging at 5000 revolutions per minute (rpm) for 10 min at 4°C. After enzymatic digestion, shearing, and 0.5 M EDTA blocking, the sheared chromatin was incubated with proper antibody and magnetic beads on rotator at 4°C overnight. After wash and reverse cross-link, DNA was purified by using DNA Fragment purification kit (9761, Takara, Shiga, Japan) and quantified by RT-qPCR with specific primers (the primers used were listed in table S8). Results are presented as the percentage of the total input DNA [% input = 100 × 2^ (adjusted C_t of input − C_t of IP samples), adjusted C_t of input = C_t of input − $\log_2$ dilution factor].

ChIP-seq

ChIP-seq library preparation and data analysis were performed by Active Motif (Shanghai, China). In brief, cells were cross-linked with 1% formaldehyde and quenched with 125 mM glycine. The chromatin fragments were precleared and then immunoprecipitated with Protein G Magnetic Beads coupled with anti-PHF8 (A301-772A, Bethyl Laboratories) and anti c-MYC (9402, Cell Signaling Technology) antibodies. After reverse cross-linking, ChIP and input DNA fragments were end-repaired and A-tailed using the

NEBNext End Repair/dA-Tailing Module [E7442, New England Biolabs (NEB)], followed by adaptor ligation with the NEBNext Ultra Ligation Module (E7445, NEB). The DNA libraries were amplified for 15 cycles and sequenced using Illumina NextSeq 500 with single-end 1 × 75 as the sequencing mode. Raw reads were filtered to obtain high-quality clean reads by removing sequencing adapters, short reads (length: <35 base pairs), and low-quality reads using Cutadapt (v1.9.1) and Trimmomatic (v0.35). Then, FastQC is used to ensure high-quality reads. The clean reads were mapped to the human genome (assembly human genome GRCh38) using the Burrows-Wheeler Aligner software (*63*). Peak detection was performed using the MACS (v2.1.1) peak finding algorithm (*64*) with 0.05 set as the *q* value cutoff. Annotation of peak sites to gene features was performed using the ChIPseeker R package (*65*).

CoIP and immunoblotting

For CoIP, protein was extracted by Pierce IP Lysis Buffer (87787, Thermo Fisher Scientific) with cOmplete Tablets, Mini EDTA-free, EASYpack (04693159001, Roche, Basel, Switzerland), and PhosSTOP EASYpack (04906837001, Roche). Briefly, the lysates were incubated with certain antibodies at 4°C overnight. Then, lysates were incubated with Pierce Protein A Magnetic Beads (88846, Thermo Fisher Scientific) for an hour at room temperature. After being washed by lysis buffer, beads were heated with SDS loading and analyzed by WB. Antibodies used in this study were listed in table S6.

Western blotting

Cultured cells or tumor tissues and matched normal tissues from patients with ccRCC were lysed with T-PER Tissue Protein Extraction Reagent (78510, Thermo Fisher Scientific) and a mixture of cOmplete Tablets, Mini EDTA-free, EASYpack, and PhosSTOP EASYpack. After centrifugation at 12,000 rpm and 4°C for 15 min, the supernatant of lysates was collected for WB according to standard procedures. Antibodies used in this study listed in table S6. Detection was performed by measuring chemiluminescence on ChemiDoc XRS+ System (Bio-Rad, Hercules, CA, USA).

IHC staining

All fresh specimens were fixed in 4% paraformaldehyde (PFA) for 24 hours, embedded by paraffin, and sectioned (3 μm) for staining according to the procedure of previous study (*31*, *66*). In brief, antigen retrieval was performed by boiling slides in citrate (MVS-0101, MaxVision, Fuzhou, China) or EDTA solution (MVS-0099, MaxVision) according to instruction of antibodies (table S6). Slides were blocked with 5% goat serum and incubated with primary antibody at 4°C overnight and secondary antibodies anti-mouse/rabbit (Kit-5030, MaxVision) for 30 min. Then, the antigens were stained by 3,30-diaminobenzidine. The stained slices were photographed under a light microscope (Olympus, BX53). Then, staining intensities were scored by certified urological pathologists (Q. Ma and P. Zhong) as described previously (*67*).

ORO staining

For ORO staining (S19039, Shanghai Yuanye Bio-Technology, Shanghai, China), fresh frozen tissues were sectioned at a thickness of 10 μm or cells were seeded on a six-well plate containing glass coverslips. In brief, frozen tissues or cells were fixed in 4% PFA for 15 min and washed three times with PBS. Then, lipid droplets in cells were stained with ORO working solution (ORO dissolved in 60% isopropanol and 40% water, v/v) for 30 min in room temperature. Specimens were rinsed with PBS for three times and stained with Mayer′s hematoxylin for 5 min. The stained slices were photographed by using microscope (Olympus, BX53), and lipid droplets were quantified by using the ImageJ software (Fiji).

BODIPY 493/503 staining

Briefly, after culturing on glass coverslips in a six-well plate, cells were fixed in 4% PFA for 10 min, washed three times with PBS, and then stained with BODIPY 493/503 (2 μM) for 30 min at room temperature in dark room. Cells were then again washed three times with PBS, followed by DAPI (4i,6-diamidino-2-phenylindole) incubation for 5 min. Lipid droplets were visualized using a microscope (Olympus, BX53). For organoids staining, lipid droplets were visualized using Zeiss laser scanning confocal microscope (LSM 880, Carl Zeiss, Jena, Germany). Lipid droplets were quantified by using the ImageJ software (Fiji).

Glutamine and triglyceride quantitation assay

In brief, 1×10^4 cells were seeded in 96-well plate and incubated overnight. Then, culture medium was removed, and cells were washed with PBS three times. Then, cells were treated with Glutamine/Glutamate-Glo-Assay (J8021) or Triglyceride-Glo Assay (J3160) according to the manufacturer′s instruction. Detection was performed by measuring chemiluminescence on SpectraMax iD3 spectrophotometer (Molecular Devices, San Jose, CA, USA).

Lipidomic analysis

The 0.75-ml iced methanol and 2.5 ml of methyl tert-butyl ether was added into 100 μl of sample. The mixture was incubated for an hour at room temperature in a shaker. The 0.625-ml mass spectrometry (MS)–grade water was added to induce phase separation, and then the mixture was centrifuged at 1000*g* for 10 min. The upper (organic) phase was collected. After quality control, ultra-high-performance liquid chromatography (UHPLC)–tandem MS (MS/MS) analyses were performed using a Vanquish UHPLC system (Thermo Fisher Scientific, Germany) coupled with an Orbitrap Q Exactive HF mass spectrometer (Thermo Fisher Scientific, Germany) in Novogene Co. Ltd. (Beijing, China). The raw data files generated by UHPLC-MS/MS were processed using the Compound Discoverer 3.01 (CD3.1, Thermo Fisher Scientific) to perform peak alignment, peak picking, and quantitation for each metabolite. Peaks were matched with the LIPID MAPS, LipidBlast, and Human Metabolome Database. After statistical analyses using statistical software R (version R-3.4.3), Python (Python 2.7.6), and CentOS (CentOS 6.6 release), the metabolites with $P < 0.05$ and FC of ≥ 2 or ≤ 0.5 were considered to be differential metabolites.

Carbon metabolite analysis

Using glutamine-free DMEM (11960044, Gibco) supplemented with 500 μM [$^{13}C_5$]-L-glutamic acid (IR-30570, IsoReag, Shanghai Zzbio Co. Ltd.) and 10% FBS, we labeled 786-O cells (transfected with siRNA targeting *GLUL* or scrambled siRNA) for 24 hours. After washing and metabolites extraction, clear supernatant was collected and analyzed by Dionex ICS-6000 high-performance ion exchange chromatography–MS/MS (HPIC-MS/MS) with the method developed by Shanghai Biotree Biomedical Technology Co. Ltd. (Shanghai, China) (*68*). Briefly, cells were washed with ice-cold normal saline and extracted with 500 μl of extract solvent (MeOH/H2O, 3:1, precooled at −40°C). After vortexing for 30 s, the samples were homogenized for 4 min at 35 Hz with a shaking table. The homogenized tissue extract was sonicated in ice water bath for 5 min, followed by incubation at −40°C for 1 hour and centrifugation at 12000 rpm at 4°C for 15 min. The supernatant was collected and analyzed by HPIC-MS/MS. Standard solutions of metabolites were used for calibration of PIC-MS/MS.

Colony formation assay

Cells in logarithmic growth phase were digested with 0.25% trypsin (03-050-1ACS, Biological Industries), centrifuged, and counted after resuspending. About 1000 cells were seeded in each well of six-well plate. After 2 weeks, six-well plate was harvested by rinsing with PBS for three times, fixing with 4% PFA for 10 min. Colonies were stained with crystal violet (0.5%, C0121, Beyotime) for 2 min, and the numbers of colonies were counted by using ImageJ software.

CCK-8 assay

Cells were seeded into 96-well plate at a density of 1×10^3 cells per well with 100 μl of complete medium. To evaluate cell viability, cell counting kit-8 (CCK-8) was added into each well and incubated for 2 hours at 37°C under 5% CO_2. The absorbance was read at 450 nm by using SpectraMax iD3 spectrophotometer (Molecular Devices).

EdU assay

Cells were seeded into a six-well plate with glass coverslips and cultured overnight in complete medium. EdU cell proliferation kit (C0071S, Beyotime, Shanghai, China) was used according to the manufacturer′s instruction. Briefly, cells were treated with 1× EdU for 2 hours. Then, DAPI was used to dye the cell nucleus. The stained cells were photographed by using fluorescence microscope (Olympus, BX53) and analyzed by using ImageJ software.

Flow cytometry

Cell lipid content was measured by flow cytometry using the BODIPY 493/503 probe. Briefly, cells were transfected with siRNA targeting *PHF8*, *JARID1A*, *JARID1C*, *JHDM1A*, *JHDM2A*, and *UTX*, *PHF2*, and scrambled siRNA were stained by BODIPY 493/503 for 30 min at room temperature. Cells were collected and washed with PBS for three times and subsequently resuspended with PBS. All cells were analyzed on a CytoFLEX (Beckman Coulter, Indianapolis, IN, USA) flow cytometer to measure the fluorescence intensity.

Dual-luciferase reporter assay

HEK293T cells were seeded in 24-well plates at a density of 1×10^5 cells per well. When confluence reached 70 to 80%, cells were co-transfected with 500 ng of plasmid (Flag-*HIF1A*, MYC-*HIF2A*, *YAP1*, *c-MYC*, *PHF8*, or $PHF8^{H283A}$) and promoter plasmid (*PHF8*, *TEAD1*, and *GLUL*) containing reporters (firefly luciferase and Renilla luciferase) in presence of ViaFect (Promega). Luciferase activities were measured at 48 hours after transfection using the Luc-Pair™ Duo-Luciferase HS Assay Kit (GeneCopoeia, cat. no. LF004) according to the manufacturer′s instruction and were normalized to Renilla luciferase activities.

Gene set enrichment analysis

GSEA (www.gsea-msigdb.org/gsea/index.jsp) was performed to analyze the datasets involved in HALLMARK_MYC_TARGETS_V2 and Hippo signaling pathway defined by KEGG. Genes were preranked according to their expression of RNA-seq, and R package clusterProfiler 4.4.4 was used for GSEA analysis and visualization (*69*).

Clinical outcome

For TMA analysis, the immunohistochemically stained tissue sections were scored separately by two urological pathologists (Q. Ma and P. Zhong) blinded to the clinicopathological parameters. Briefly, the quantified method is based on a multiplicative index of the average staining intensity (0 to 3) and extent of staining (0 to 3) in the cores. The staining score of ≤4 was defined as low expression, whereas the score of >4 was referred as high expression. TMA data and clinical information were used for analyses, and survival analysis was performed using Kaplan-Meier method. The hazard ratio and confidence intervals (CIs; 95% CI) were computed.

Statistical analysis

Unless otherwise specified in the figure legends, all experiments reported in this study were performed using at least three independent experiments or biological replicates. Analysis for the statistical significance between two groups were determined by two-tailed Student′s *t* test, analysis of variance (ANOVA), Pearson correlation, log-rank test, Fisher′s exact test, or Wilcoxon rank sum test. For all statistical tests, the 0.05 level of confidence was accepted for statistical significance.

Supplementary Materials

This PDF file includes:

Figs. S1 to S8

Legends for tables S1 to S8

Other Supplementary Material for this manuscript includes the following:

Tables S1 to S8

REFERENCES AND NOTES

1. H. Sung, J. Ferlay, R. L. Siegel, M. Laversanne, I. Soerjomataram, A. Jemal, F. Bray, Global cancer statistics 2020: GLOBOCAN estimates of incidence and mortality worldwide for 36 cancers in 185 countries. *CA Cancer J. Clin.* **71**, 209–249 (2021).
2. A. A. Hakimi, E. Reznik, C. H. Lee, C. J. Creighton, A. R. Brannon, A. Luna, B. A. Aksoy, E. M. Liu, R. Shen, W. Lee, Y. Chen, S. M. Stirdivant, P. Russo, Y. B. Chen, S. K. Tickoo, V. E. Reuter, E. H. Cheng, C. Sander, J. J. Hsieh, An integrated metabolic atlas of clear cell renal cell carcinoma. *Cancer Cell* **29**, 104–116 (2016).
3. G. Heravi, O. Yazdanpanah, I. Podgorski, L. H. Matherly, W. Liu, Lipid metabolism reprogramming in renal cell carcinoma. *Cancer Metastasis Rev.* **41**, 17–31 (2022).
4. X. Bian, R. Liu, Y. Meng, D. Xing, D. Xu, Z. Lu, Lipid metabolism and cancer. *J. Exp. Med.* **218**, e20201606 (2021).
5. H. Iwamoto, M. Abe, Y. Yang, D. Cui, T. Seki, M. Nakamura, K. Hosaka, S. Lim, J. Wu, X. He, X. Sun, Y. Lu, Q. Zhou, W. Shi, T. Torimura, G. Nie, Q. Li, Y. Cao, Cancer lipid metabolism confers antiangiogenic drug resistance. *Cell Metab.* **28**, 104–117.e5 (2018).
6. M. L. Nickerson, E. Jaeger, Y. Shi, J. A. Durocher, S. Mahurkar, D. Zaridze, V. Matveev, V. Janout, H. Kollarova, V. Bencko, M. Navratilova, N. Szeszenia-Dabrowska, D. Mates, A. Mukeria, I. Holcatova, L. S. Schmidt, J. R. Toro, S. Karami, R. Hung, G. F. Gerard, W. M. Linehan, M. Merino, B. Zbar, P. Boffetta, P. Brennan, N. Rothman, W. H. Chow, F. M. Waldman, L. E. Moore, Improved identification of von Hippel-Lindau gene alterations in clear cell renal tumors. *Clin. Cancer Res.* **14**, 4726–4734 (2008).
7. L. Gossage, T. Eisen, E. R. Maher, VHL, the story of a tumour suppressor gene. *Nat. Rev. Cancer* **15**, 55–64 (2015).
8. P. A. Gameiro, J. Yang, A. M. Metelo, R. Pérez-Carro, R. Baker, Z. Wang, A. Arreola, W. K. Rathmell, A. Olumi, P. López-Larrubia, G. Stephanopoulos, O. Iliopoulos, In vivo HIF-mediated reductive carboxylation is regulated by citrate levels and sensitizes VHL-deficient cells to glutamine deprivation. *Cell Metab.* **17**, 372–385 (2013).
9. H. I. Wettersten, O. A. Aboud, P. N. Lara Jr., R. H. Weiss, Metabolic reprogramming in clear cell renal cell carcinoma. *Nat. Rev. Nephrol.* **13**, 410–419 (2017).
10. W. Du, L. Zhang, A. Brett-Morris, B. Aguila, J. Kerner, C. L. Hoppel, M. Puchowicz, D. Serra, L. Herrero, B. I. Rini, S. Campbell, S. M. Welford, HIF drives lipid deposition and cancer in ccRCC via repression of fatty acid metabolism. *Nat. Commun.* **8**, 1769 (2017).
11. B. J. Altman, Z. E. Stine, C. V. Dang, From Krebs to clinic: Glutamine metabolism to cancer therapy. *Nat. Rev. Cancer* **16**, 749 (2016).
12. A. Halama, K. Suhre, Advancing cancer treatment by targeting glutamine metabolism–A roadmap. *Cancers (Basel)* **14**, 553 (2022).
13. R. J. DeBerardinis, T. Cheng, Q's next: The diverse functions of glutamine in metabolism, cell biology and cancer. *Oncogene* **29**, 313–324 (2010).
14. C. M. Metallo, P. A. Gameiro, E. L. Bell, K. R. Mattaini, J. Yang, K. Hiller, C. M. Jewell, Z. R. Johnson, D. J. Irvine, L. Guarente, J. K. Kelleher, M. G. Vander Heiden, O. Iliopoulos, G. Stephanopoulos, Reductive glutamine metabolism by IDH1 mediates lipogenesis under hypoxia. *Nature* **481**, 380–384 (2011).

15. S. Tardito, A. Oudin, S. U. Ahmed, F. Fack, O. Keunen, L. Zheng, H. Miletic, P. Ø. Sakariassen, A. Weinstock, A. Wagner, S. L. Lindsay, A. K. Hock, S. C. Barnett, E. Ruppin, S. H. Mørkve, M. Lund-Johansen, A. J. Chalmers, R. Bjerkvig, S. P. Niclou, E. Gottlieb, Glutamine synthetase activity fuels nucleotide biosynthesis and supports growth of glutamine-restricted glioblastoma. *Nat. Cell Biol.* **17**, 1556–1568 (2015).
16. A. J. Bott, I. C. Peng, Y. Fan, B. Faubert, L. Zhao, J. Li, S. Neidler, Y. Sun, N. Jaber, D. Krokowski, W. Lu, J. A. Pan, S. Powers, J. Rabinowitz, M. Hatzoglou, D. J. Murphy, R. Jones, S. Wu, G. Girnun, W. X. Zong, Oncogenic Myc induces expression of glutamine synthetase through promoter demethylation. *Cell Metab.* **22**, 1068–1077 (2015).
17. J. Zhang, N. N. Pavlova, C. B. Thompson, Cancer cell metabolism: The essential role of the nonessential amino acid, glutamine. *EMBO J.* **36**, 1302–1315 (2017).
18. A. J. Bott, J. Shen, C. Tonelli, L. Zhan, N. Sivaram, Y. P. Jiang, X. Yu, V. Bhatt, E. Chiles, H. Zhong, S. Maimouni, W. Dai, S. Velasquez, J. A. Pan, N. Muthalagu, J. Morton, T. G. Anthony, H. Feng, W. H. Lamers, D. J. Murphy, J. Y. Guo, J. Jin, H. C. Crawford, L. Zhang, E. White, R. Z. Lin, X. Su, D. A. Tuveson, W. X. Zong, Glutamine anabolism plays a critical role in pancreatic cancer by coupling carbon and nitrogen metabolism. *Cell Rep.* **29**, 1287–1298.e6 (2019).
19. Cancer Genome Atlas Research, Comprehensive molecular characterization of clear cell renal cell carcinoma. *Nature* **499**, 43–49 (2013).
20. X. Xia, M. E. Lemieux, W. Li, J. S. Carroll, M. Brown, X. S. Liu, A. L. Kung, Integrative analysis of HIF binding and transactivation reveals its role in maintaining histone methylation homeostasis. *Proc. Natl. Acad. Sci. U.S.A.* **106**, 4260–4265 (2009).
21. C. Shen, W. G. Kaelin Jr., The VHL/HIF axis in clear cell renal carcinoma. *Semin. Cancer Biol.* **23**, 18–25 (2013).
22. K. Fortschegger, R. Shiekhattar, Plant homeodomain fingers form a helping hand for transcription. *Epigenetics* **6**, 4–8 (2011).
23. S. S. Chaturvedi, R. Ramanan, S. O. Waheed, T. G. Karabencheva-Christova, C. Z. Christov, Structure-function relationships in KDM7 histone demethylases. *Adv. Protein Chem. Struct. Biol.* **117**, 113–125 (2019).
24. J. Qiu, G. Shi, Y. Jia, J. Li, M. Wu, J. Li, S. Dong, J. Wong, The X-linked mental retardation gene PHF8 is a histone demethylase involved in neuronal differentiation. *Cell Res.* **20**, 908–918 (2010).
25. X. Chen, S. Wang, Y. Zhou, Y. Han, S. Li, Q. Xu, L. Xu, Z. Zhu, Y. Deng, L. Yu, L. Song, A. P. Chen, J. Song, E. Takahashi, G. He, L. He, W. Li, C. D. Chen, Phf8 histone demethylase deficiency causes cognitive impairments through the mTOR pathway. *Nat. Commun.* **9**, 114 (2018).
26. E. Asensio-Juan, C. Gallego, M. A. Martinez-Balbas, The histone demethylase PHF8 is essential for cytoskeleton dynamics. *Nucleic Acids Res.* **40**, 9429–9440 (2012).
27. Q. Wang, S. Ma, N. Song, X. Li, L. Liu, S. Yang, X. Ding, L. Shan, X. Zhou, D. Su, Y. Wang, Q. Zhang, X. Liu, N. Yu, K. Zhang, Y. Shang, Z. Yao, L. Shi, Stabilization of histone demethylase PHF8 by USP7 promotes breast carcinogenesis. *J. Clin. Invest.* **126**, 2205–2220 (2016).
28. M. Li, Q. Chen, X. Yu, Chemopreventive effects of ROS targeting in a murine model of BRCA1-deficient breast cancer. *Am. J. Cancer Res.* **77**, 448–458 (2017).
29. W. Zhou, L. Gong, Q. Wu, C. Xing, B. Wei, T. Chen, Y. Zhou, S. Yin, B. Jiang, H. Xie, L. Zhou, S. Zheng, PHF8 upregulation contributes to autophagic degradation of E-cadherin, epithelial-mesenchymal transition and metastasis in hepatocellular carcinoma. *J. Exp. Clin. Cancer Res.* **37**, 215 (2018).
30. Y. Fu, Y. Yang, X. Wang, X. Yin, M. Zhou, S. Wang, L. Yang, T. Huang, M. Xu, C. Chen, The histone demethylase PHF8 promotes adult acute lymphoblastic leukemia through interaction with the MEK/ERK signaling pathway. *Biochem. Biophys. Res. Commun.* **496**, 981–987 (2018).
31. Q. Liu, J. Pang, L. A. Wang, Z. Huang, J. Xu, X. Yang, Q. Xie, Y. Huang, T. Tang, D. Tong, G. Liu, L. Wang, D. Zhang, Q. Ma, H. Xiao, W. Lan, J. Qin, J. Jiang, Histone demethylase PHF8 drives neuroendocrine prostate cancer progression by epigenetically upregulating FOXA2. *J. Pathol.* **253**, 106–118 (2021).
32. B. Qiu, D. Ackerman, D. J. Sanchez, B. Li, J. D. Ochocki, A. Grazioli, E. Bobrovnikova-Marjon, J. A. Diehl, B. Keith, M. C. Simon, HIF2α-dependent lipid storage promotes endoplasmic reticulum homeostasis in clear-cell renal cell carcinoma. *Cancer Discov.* **5**, 652–667 (2015).
33. Y. Du, Q. Wang, X. Zhang, X. Wang, C. Qin, Z. Sheng, H. Yin, C. Jiang, J. Li, T. Xu, Lysophosphatidylcholine acyltransferase 1 upregulation and concomitant phospholipid alterations in clear cell renal cell carcinoma. *J. Exp. Clin. Cancer Res.* **36**, 66 (2017).
34. P. F. Karmokar, N. H. Moniri, Oncogenic signaling of the free-fatty acid receptors FFA1 and FFA4 in human breast carcinoma cells. *Biochem. Pharmacol.* **206**, 115328 (2022).
35. Z. Liu, M. M. Hopkins, Z. Zhang, C. B. Quisenberry, L. C. Fix, B. M. Galvan, K. E. Meier, Omega-3 fatty acids and other FFA4 agonists inhibit growth factor signaling in human prostate cancer cells. *J. Pharmacol. Exp. Ther.* **352**, 380–394 (2015).
36. J. Wang, X. Lin, S. Wang, C. Wang, Q. Wang, X. Duan, P. Lu, Q. Wang, C. Wang, X. S. Liu, J. Huang, PHF8 and REST/NRSF co-occupy gene promoters to regulate proximal gene expression. *Sci. Rep.* **4**, 5008 (2014).
37. A. G. Cox, K. L. Hwang, K. K. Brown, K. J. Evason, S. Beltz, A. Tsomides, K. O'Connor, G. G. Galli, D. Yimlamai, S. Chhangawala, M. Yuan, E. C. Lien, J. Wucherpfennig, S. Nissim, A. Minami, D. E. Cohen, F. D. Camargo, J. M. Asara, Y. Houvras, D. Y. R. Stainier, W. Goessling, Yap reprograms glutamine metabolism to increase nucleotide biosynthesis and enable liver growth. *Nat. Cell Biol.* **18**, 886–896 (2016).
38. V. Tambay, V. A. Raymond, M. Bilodeau, MYC rules: Leading glutamine metabolism toward a distinct cancer cell phenotype. *Cancers (Basel)* **13**, 4484 (2021).
39. D. S. Chandrashekar, B. Bashel, S. A. H. Balasubramanya, C. J. Creighton, I. Ponce-Rodriguez, B. V. S. K. Chakravarthi, S. Varambally, UALCAN: A portal for facilitating tumor subgroup gene expression and survival analyses. *Neoplasia* **19**, 649–658 (2017).
40. K. E. van der Vos, P. Eliasson, T. Proikas-Cezanne, S. J. Vervoort, R. van Boxtel, M. Putker, I. J. van Zutphen, M. Mauthe, S. Zellmer, C. Pals, L. P. Verhagen, M. J. A. G. Koerkamp, A. K. Braat, T. B. Dansen, F. C. Holstege, R. Gebhardt, B. M. Burgering, P. J. Coffer, Modulation of glutamine metabolism by the PI(3)K-PKB-FOXO network regulates autophagy. *Nat. Cell Biol.* **14**, 829–837 (2012).
41. W. Dai, J. Shen, J. Yan, A. J. Bott, S. Maimouni, H. Q. Daguplo, Y. Wang, K. Khayati, J. Y. Guo, L. Zhang, Y. Wang, A. Valvezan, W. X. Ding, X. Chen, X. Su, S. Gao, W. X. Zong, Glutamine synthetase limits β-catenin–mutated liver cancer growth by maintaining nitrogen homeostasis and suppressing mTORC1. *J. Clin. Invest.* **132**, e161408 (2022).
42. L. A. Broadfield, A. A. Pane, A. Talebi, J. V. Swinnen, S. M. Fendt, Lipid metabolism in cancer: New perspectives and emerging mechanisms. *Dev. Cell* **56**, 1363–1393 (2021).
43. Y. Y. Qu, R. Zhao, H. L. Zhang, Q. Zhou, F. J. Xu, X. Zhang, W. H. Xu, N. Shao, S. X. Zhou, B. Dai, Y. Zhu, G. H. Shi, Y. J. Shen, Y. P. Zhu, C. T. Han, K. Chang, Y. Lin, W. D. Zang, W. Xu, D. W. Ye, S. M. Zhao, J. Y. Zhao, Inactivation of the AMPK-GATA3-ECHS1 pathway induces fatty acid synthesis that promotes clear cell renal cell carcinoma growth. *Cancer Res.* **80**, 319–333 (2020).
44. X. Li, Z. Liu, C. Xia, K. Yan, Z. Fang, Y. Fan, SETD8 stabilized by USP17 epigenetically activates SREBP1 pathway to drive lipogenesis and oncogenesis of ccRCC. *Cancer Lett.* **527**, 150–163 (2022).
45. G. Lucarelli, M. Ferro, D. Loizzo, C. Bianchi, D. Terracciano, F. Cantiello, L. N. Bell, S. Battaglia, C. Porta, A. Gernone, R. A. Perego, E. Maiorano, O. de Cobelli, G. Castellano, L. Vincenti, P. Ditonno, M. Battaglia, Integration of lipidomics and transcriptomics reveals reprogramming of the lipid metabolism and composition in clear cell renal cell carcinoma. *Metabolites* **10**, 509 (2020).
46. X. Zhang, A. M. Saarinen, T. Hitosugi, Z. Wang, L. Wang, T. H. Ho, J. Liu, Inhibition of intracellular lipolysis promotes human cancer cell adaptation to hypoxia. *eLife* **6**, e31132 (2017).
47. G. W. Kim, D. H. Lee, Y. H. Jeon, J. Yoo, S. Y. Kim, S. W. Lee, H. Y. Cho, S. H. Kwon, Glutamine synthetase as a therapeutic target for cancer treatment. *Int. J. Mol. Sci.* **22**, (2021).
48. M. Kodama, K. Oshikawa, H. Shimizu, S. Yoshioka, M. Takahashi, Y. Izumi, T. Bamba, C. Tateishi, T. Tomonaga, M. Matsumoto, K. I. Nakayama, A shift in glutamine nitrogen metabolism contributes to the malignant progression of cancer. *Nat. Commun.* **11**, 1320 (2020).
49. H. Sun, C. Zhang, Y. Zheng, C. Liu, X. Wang, X. Cong, Glutamine deficiency promotes recurrence and metastasis in colorectal cancer through enhancing epithelial-mesenchymal transition. *J. Transl. Med.* **20**, 330 (2022).
50. X. Chen, R. Kang, G. Kroemer, D. Tang, Broadening horizons: The role of ferroptosis in cancer. *Nat. Rev. Clin. Oncol.* **18**, 280–296 (2021).
51. E. C. Lien, C. A. Lyssiotis, A. Juvekar, H. Hu, J. M. Asara, L. C. Cantley, A. Toker, Glutathione biosynthesis is a metabolic vulnerability in PI(3)K/Akt-driven breast cancer. *Nat. Cell Biol.* **18**, 572–578 (2016).
52. Y. Zheng, D. Pan, The hippo signaling pathway in development and disease. *Dev. Cell* **50**, 264–282 (2019).
53. H. D. Huh, D. H. Kim, H. S. Jeong, H. W. Park, Regulation of TEAD transcription factors in cancer biology. *Cell* **8**, 600 (2019).
54. J. S. Wong, K. Meliambro, J. Ray, K. N. Campbell, Hippo signaling in the kidney: The good and the bad. *Am. J. Physiol. Renal Physiol.* **311**, F241–F248 (2016).
55. P. Carter, U. Schnell, C. Chaney, B. Tong, X. Pan, J. Ye, G. Mernaugh, J. L. Cotton, V. Margulis, J. Mao, R. Zent, B. M. Evers, P. Kapur, T. J. Carroll, Deletion of Lats1/2 in adult kidney epithelia leads to renal cell carcinoma. *J. Clin. Invest.* **131**, e144108 (2021).
56. B. C. Grieb, C. M. Eischen, MTBP and MYC: A dynamic duo in proliferation, cancer, and aging. *Biology (Basel)* **11**, 881 (2022).
57. G. Svenneby, I. A. Torgner, Localization and function of glutamine synthetase and glutaminase. *Biochem. Soc. Trans.* **15**, 213–215 (1987).
58. J. W. Jhu, J. B. Yan, Z. H. Lin, S. C. Lin, I. C. Peng, SREBP1-induced glutamine synthetase triggers a feedforward loop to upregulate SREBP1 through Sp1 O-GlcNAcylation and augments lipid droplet formation in cancer cells. *Int. J. Mol. Sci.* **22**, 9814 (2021).
59. L. Grassi, R. Alfonsi, F. Francescangeli, M. Signore, M. L. de Angelis, A. Addario, M. Costantini, E. Flex, A. Ciolfi, S. Pizzi, A. Bruselles, M. Pallocca, G. Simone, M. Haoui, M. Falchi, M. Milella,

S. Sentinelli, P. di Matteo, E. Stellacci, M. Gallucci, G. Muto, M. Tartaglia, R. de Maria, D. Bonci, Organoids as a new model for improving regenerative medicine and cancer personalized therapy in renal diseases. *Cell Death Dis.* **10**, 201 (2019).

60. J. C. Na, J. H. Kim, S. Y. Kim, Y. R. Gu, D. Y. Jun, H. H. Lee, Y. E. Yoon, K. H. Choi, S. J. Hong, W. K. Han, Establishment of patient-derived three-dimensional organoid culture in renal cell carcinoma. *Investig. Clin. Urol.* **61**, 216–223 (2020).
61. D. Kim, B. Langmead, S. L. Salzberg, HISAT: A fast spliced aligner with low memory requirements. *Nat. Methods* **12**, 357–360 (2015).
62. M. I. Love, W. Huber, S. Anders, Moderated estimation of fold change and dispersion for RNA-seq data with DESeq2. *Genome Biol.* **15**, 550 (2014).
63. H. Li, R. Durbin, Fast and accurate long-read alignment with Burrows-Wheeler transform. *Bioinformatics* **26**, 589–595 (2010).
64. J. Feng, T. Liu, B. Qin, Y. Zhang, X. S. Liu, Identifying ChIP-seq enrichment using MACS. *Nat. Protoc.* **7**, 1728–1740 (2012).
65. G. Yu, L. G. Wang, Q. Y. He, ChIPseeker: An R/Bioconductor package for ChIP peak annotation, comparison and visualization. *Bioinformatics* **31**, 2382–2383 (2015).
66. D. Tong, Q. Liu, G. Liu, J. Xu, W. Lan, Y. Jiang, H. Xiao, D. Zhang, J. Jiang, Metformin inhibits castration-induced EMT in prostate cancer by repressing COX2/PGE2/STAT3 axis. *Cancer Lett.* **389**, 23–32 (2017).
67. Q. Liu, D. Tong, G. Liu, J. Gao, L. A. Wang, J. Xu, X. Yang, Q. Xie, Y. Huang, J. Pang, L. Wang, Y. He, D. Zhang, Q. Ma, W. Lan, J. Jiang, Metformin inhibits prostate cancer progression by targeting tumor-associated inflammatory infiltration. *Clin. Cancer Res.* **24**, 5622–5634 (2018).
68. C. Sun, Y. Zhang, M. Liu, Z. Liu, L. Pan, H. Liang, N. Liu, S. Li, D. Niu, X. Li, B. Li, L. Cui, J. Yao, X. Xiao, G. Zhang, Shouhui Tongbian Capsules induce regression of inflammation to improve intestinal barrier in mice with constipation by targeted binding to Prkaa1: With no obvious toxicity. *Biomed. Pharmacother.* **161**, 114495 (2023).
69. T. Wu, E. Hu, S. Xu, M. Chen, P. Guo, Z. Dai, T. Feng, L. Zhou, W. Tang, L. Zhan, X. Fu, S. Liu, X. Bo, G. Yu, clusterProfiler 4.0: A universal enrichment tool for interpreting omics data. *Innovation (Camb)* **2**, 100141 (2021).

Acknowledgments: We thank the patients who donated tissues that made this research possible. We also thank urological pathologists Q. Ma and P. Zhong for immunohistochemistry analyzing and scoring. **Funding:** This work was supported by the National Natural Science Foundation of China (grant no: 82172807 and 81972398 for J.J. and 82172721 for Q.L.), University Research Project of Army Medical University (2018XLC1014 and 2019CXLCB006 for J.J. and 2021XQN24 for Q.L.), and National Key Research and Development Program of China (no. 2022YFA1105300 for B.W.). **Author contributions:** Conceptualization: Q.L., J.J., and J.Q. Methodology: S.P., Q.L., J.J., and B.W. Cell culture and experiments: S.P., Z.W., S.W., Y.H., Q.X., and Y.W. Mouse feeding and experiments: S.P., Q.X., T.T., X.T., J.X., and Y.W. Organoid generation and experiments: P.T. and S.P. Patient samples and analysis: S.P., Q.L., and S.W. Data interpreting and analyzing: S.P., Z.W., P.T., Q.L., and Y.W. Visualization: S.P. and X.Y. Manuscript drafting: S.P. Manuscript revising: Q.L., J.J., D.Z., B.W., J.Q., T.P., Z.W., L.W., W.L., and T.P. Supervision: Q.L., J.J., and J.Q. **Competing interests:** The authors declare that they have no competing interests. **Data and materials availability:** All data needed to evaluate the conclusions in the paper are present in the paper and/or the Supplementary Materials. RNA-seq and ChIP-seq raw data have been deposited in Gene Expression Omnibus (https://ncbi.nlm.nih.gov/geo/) with accession numbers GSE214183 and GSE217161, respectively. Lipidomic raw data have been deposited in MetaboLights (www.ebi.ac.uk/metabolights/index) with accession number MTBLS5987.

Submitted 16 October 2022
Accepted 28 June 2023
Published 2 August 2023
10.1126/sciadv.adf3566

ScienceAdvances

PHF8-GLUL axis in lipid deposition and tumor growth of clear cell renal cell carcinoma

Song Peng, Ze Wang, Peng Tang, Shuo Wang, Yiqiang Huang, Qiubo Xie, Yapeng Wang, Xintao Tan, Tang Tang, Xuzhi Yan, Jing Xu, Weihua Lan, Luofu Wang, Dianzheng Zhang, Bin Wang, Tiejun Pan, Jun Qin, Jun Jiang, and Qiuli Liu

Sci. Adv., **9** (31), eadf3566.
DOI: 10.1126/sciadv.adf3566

Science Advances (ISSN) is published by the American Association for the Advancement of Science. 1200 New York Avenue NW, Washington, DC 20005. The title *Science Advances* is a registered trademark of AAAS.